Fundamental Tests of Quantum Mechanics Using Two-Photon Entanglement

by

Lydia Vermeyden

A thesis
presented to the University of Waterloo
in fulfillment of the
thesis requirement for the degree of
Master of Science
in
Physics

Waterloo, Ontario, Canada, 2014

I hereby declare that I am the sole author of this thesis, except where noted. This is a true copy of the thesis, including any required final revisions, as accepted by my examiners.

I understand that my thesis may be made electronically available to the public.

Abstract

In this thesis, we experimentally test fundamental properties of quantum mechanics, namely non-locality (in the form of three new families of Bell's inequalities) and the symmetry of envariance. To accomplish these we use a Sagnac source of polarization entangled photon pairs.

In chapters one and two we discuss the relevant background information in quantum information theory, nonlinear optics, experimental realization of polarization entangled photons and a trouble-shooting and maintenance guide for a Saganc source.

In chapter three we experiment with a set of three newly derived families of Bell's inequalities. These three families are predicted to yield the largest volume of violation of the local hidden variable models (LHVM). Our experimental results are in good agreement with those predictions and therefore, represent the largest volume of experimental violation of LHVM to date. We showed a violation of up to 30σ from what is predicted by LHVM, and our results followed closely to the predictions of quantum mechanics.

In chapter four we experimentally test *envariance*, an assisted-symmetry exhibited by specific quantum systems. Envariance is a fundamental property in the quantum world that has lacked, until now, extensive experimental study. The symmetry has ramifications in the foundations of quantum mechanics, and plays an integral role in a proof of Born's rule [1]. Our results serve as a benchmark the property of envariance. We show that experimental quantum states can be $(99.66 \pm 0.04)\%$ envariant over a wide range of transformations, as measured using the average quantum fidelity [2], and $(99.963 \pm 0.005)\%$ as measured using a modified average Bhattacharya Coefficient [3], a measure of the overlap of two probability distributions.

Acknowledgements

First I would like to thank my supervisor Kevin Resch. He is an encouraging and diligent supervisor and I have learned an incredible amount of physics during my short time working with him. I would also like to thank the members of my advisory committee, Raymond Laflamme and David Hawthorn, and also Thomas Jennewein who is part of my examining committee. I would also like to thank the various funding agencies that made my research possible. These are Ontario Ministry of Research and Innovation ERA, QuantumWorks, NSERC, OCE, Industry Canada, Canada Research Chairs and CFI.

I would like to thank my fellow group members who worked with me in the lab over the last couple years. Many thanks to Kent Fisher who first taught me how to work a Sagnac and explained wave plates over and over and over again; to Jonathan Lavoie for teaching me the finer points of laser beam alignment and giving presentations, and working late with me to rebuild the Sagnac; to John Donohue for teaching me labview and helping me find stuff in the lab (seriously, he knows where EVERYTHING is); to Deny Hamel, the original Sagnac builder, who's wealth of knowledge on the Sagnac, and on quantum optics in general, was invaluable; to Megan Agnew for showing me how to build a displaced Sagnac interferometer (I still have mixed feelings about this setup); to Mike Mazurek for helping me with the spectrometer and explaining the whole "interferometer" thing; to Jean-Phillipe MacLean for helping me survive the quantum information processing course; to our co-op Madeleine Bonsma who was a great partner for my first experiment and inspired me to learn more Mathematica.

A special thanks goes to my family who has supported me so much throughout my university career. I would particularly like to thank my parents, who first ignited my love of science and who have been so encouraging for so long. Finally, I would like to thank my husband Bastiaan. It takes a special kind of patience to live with someone while they are writing their thesis. There are no words for how grateful I am for your unconditional support and encouragement–you never stopped believing in me.

Dedication

To the generations of feminists and female scientists that fought for gender equality in academia.

Table of Contents

List of Tables

List of Figures

Chapter 1

Background Material

1.1   Introduction

The subject of this thesis is to explore and test fundamental properties of quantum mechanics. These properties are relevant to the ideas of non-locality, local hidden variable models, and derivations of Born's rule. We use a source of polarization entangled photon pairs based on a Sagnac interferometer to create the necessary quantum states. Chapter one will cover relevant background in quantum information and non-linear optics; chapter two will discuss the mechanics and techniques associated with the entangled photon source used in all the experiments; chapters three and four will describe the experiments which implemented the source to test the fundamental properties of quantum mechanics (three parameterized families of Bell's inequalities, and the assisted-symmetry of envariance); chapter five will be the conclusion.

1.2   Defining the Qubit

A quantum bit, or qubit, is a two-level quantum system and represents the fundamental unit of information used in quantum information technologies. It differs from the classical bit, which takes the values of "zero" or "one", in that it can be either a zero, a one, or

a superposition of both. Some physical examples of qubits are nuclear spin [4], supercon-ductors [5], and single photons [6]. Physically, a qubit can be encoded in several different degrees of freedom for a photonic system: path encoding, time bins and polarization, are all examples of two-level systems in single photon states [7]. Here we represent a qubit with its general form:

$$|\psi\rangle = \alpha|0\rangle + \beta|1\rangle$$
$$\text{where, } |\alpha|^2 + |\beta|^2 = 1.$$

(1.1)

We can represent the basis states $|0\rangle$ and $|1\rangle$ (called the computational basis) with vectors $\begin{pmatrix} 1 \\ 0 \end{pmatrix}$ and $\begin{pmatrix} 0 \\ 1 \end{pmatrix}$. These are unit vectors and form an orthonormal basis in the two-dimensional Hilbert space [8].

An important way to visualize a two-level quantum state (qubit) is as a vector on the "unit sphere" or Bloch sphere [8], see Fig. 1.1. The states $|0\rangle$ and $|1\rangle$ lie on the opposite poles of the sphere, the positive and negative Z-axis respectively. The positive and negative superpositions of these states, $\frac{1}{\sqrt{2}}(|0\rangle \pm |1\rangle)$ lie along the X axis, and the equivalent imaginary superpositions, $\frac{1}{\sqrt{2}}(|0\rangle \pm i|1\rangle)$ lie along the Y axis. Unitary operations on the qubit are equivalent to rotations about the Bloch sphere

In this thesis we will be using single photons encoded in their polarization degree of freedom, where $|0\rangle$ corresponds to $|H\rangle$ or horizontally polarized, and $|1\rangle$ corresponds to $|V\rangle$, or vertically polarized. This is shown in Table 1.1 along with the other mutually unbiased polarization states. The association between polarization and the Bloch sphere comes from the Poincaré sphere [9], the original association between polarization and sphere geometry.

A pure quantum state can be described by its density matrix ρ:

$$\rho = |\psi\rangle\langle\psi|.$$

(1.2)

The density matrix can be used when applying unitaries and quantum operations. All states introduced thus far have been pure states, and as such, the representative vector on
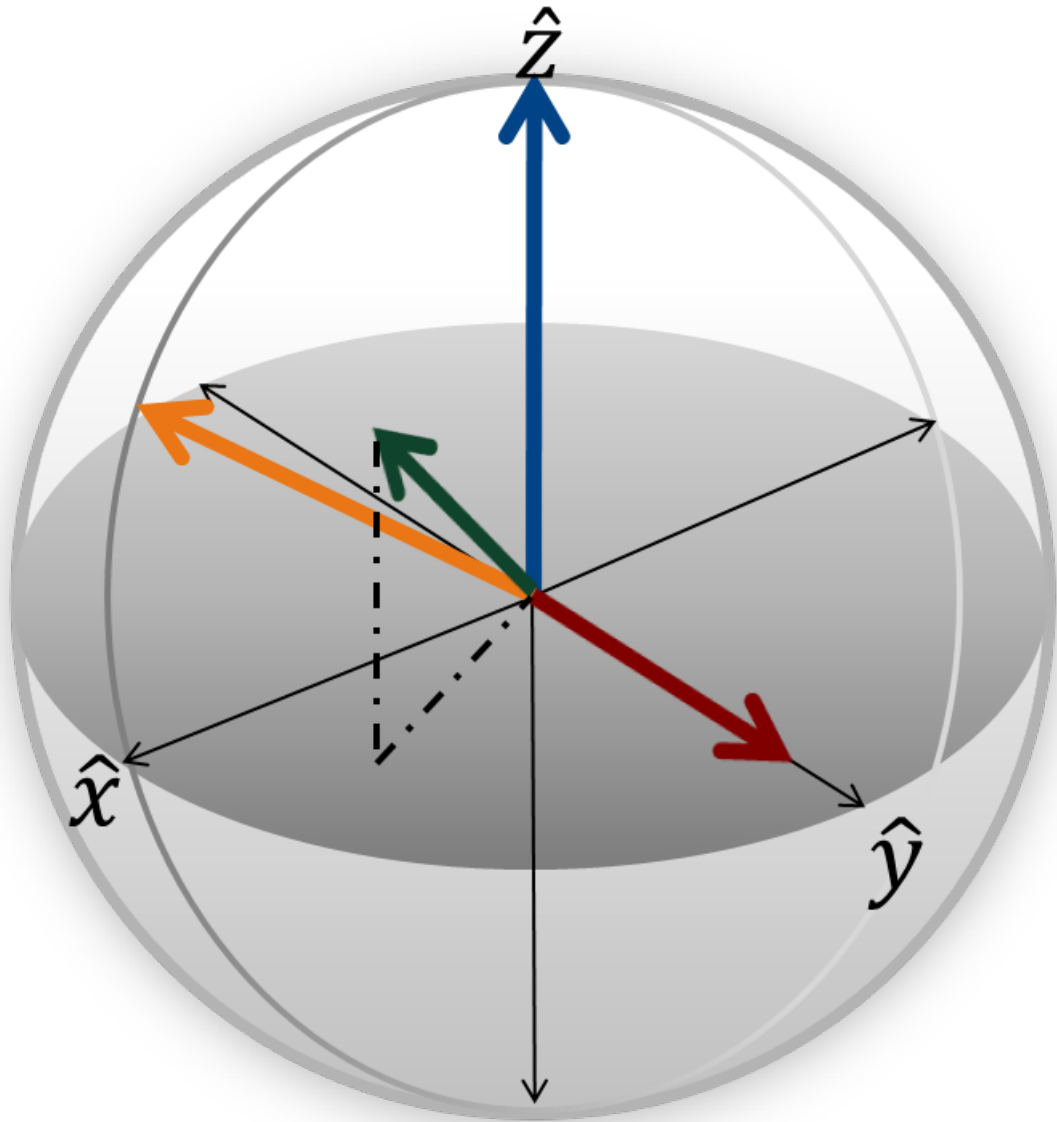
Figure 1.1: Bloch sphere representation of pure and mixed quantum states. The orange and blue vectors represent pure states which lie on the surface of the Bloch sphere, while the green and red vectors represent mixed states which lie in the interior.

Polarization	Computational Basis	Axis on the Bloch Sphere
$|H\rangle$	$|0\rangle$	$+\hat{z}$
$|V\rangle$	$|1\rangle$	$-\hat{z}$
$|D\rangle$	$\frac{1}{\sqrt{2}}(|0\rangle + |1\rangle)$	$+\hat{x}$
$|A\rangle$	$\frac{1}{\sqrt{2}}(|0\rangle - |1\rangle)$	$-\hat{x}$
$|R\rangle$	$\frac{1}{\sqrt{2}}(|0\rangle + i|1\rangle)$	$+\hat{y}$
$|L\rangle$	$\frac{1}{\sqrt{2}}(|0\rangle - i|1\rangle)$	$-\hat{y}$

Table 1.1: Definitions for the polarization basis states and their relation to the Bloch sphere.

the Bloch sphere lies on the surface of the sphere as seen in Fig. 1.1 by the orange and blue vectors. Mixed states are a probabilistic sum of pure states. Their density matrices are described as a sum:

$$\rho_{mixed} = \sum_i p_i |\psi_i\rangle\langle\psi_i|$$
$$\text{where} \sum_i p_i = 1. \tag{1.3}$$

The Bloch sphere vector representing a mixed state lies on the inside of the sphere, as seen in Fig. 1.1 by the green and red vectors. Density matrices can be used when measuring observables:

$$\langle\hat{O}\rangle = tr(\hat{\rho}\hat{O}) \tag{1.4}$$

here $\langle\hat{O}\rangle$ is the expectation value for some observable $\hat{O}$. Some important observables of two-level systems are the Pauli operators:

$$X = \begin{pmatrix} 0 & 1 \\ 1 & 0 \end{pmatrix} = \sigma_x, \quad Y = \begin{pmatrix} 0 & -i \\ i & 0 \end{pmatrix} = \sigma_y, \quad Z = \begin{pmatrix} 1 & 0 \\ 0 & -1 \end{pmatrix} = \sigma_z. \tag{1.5}$$

Measuring these Pauli observables is equivalent to measuring the projection on the respective axis on the Bloch sphere. In general, we can parameterize any density matrix in terms of the identity and the Pauli matrices [8]:

$$\rho = \frac{\mathbb{1}}{2} + \frac{c_x\sigma_x + c_y\sigma_y + c_z\sigma_z}{2}. \tag{1.6}$$

Where c_x, c_y, and c_z are the elements of the Bloch vector, $\vec{r}$:

$$\vec{r} = \begin{pmatrix} c_x \\ c_y \\ c_z \end{pmatrix}. \tag{1.7}$$

In this way, any quantum state of two dimensions can be represented in terms of its Bloch vector, or as a linear combinations of the identity and the Pauli matrices.

1.3   Two-Qubit Entanglement

Maximally entangled particles have a relationship unique to quantum mechanics in that they are so strongly correlated that they can only be described in terms of a pair of particles, not as individuals. This relationship persists regardless of spatial separation and results in complete knowledge of the state of the pair of particles, but no knowledge of the state of the individuals. Mathematically we can define a divide between entangled states and separable (non-entangled) states:

$$\rho_{separable} = \sum_k p_k \rho_1^k \otimes \rho_2^k$$
$$p_k \geq 0, \tag{1.8}$$

where $\otimes$ represents the tensor product. An entangled state cannot be written in this form, as a product of states. For pure states this reduces to:

$$|\psi_{separable}\rangle = |\psi_1\rangle \otimes |\psi_2\rangle. \tag{1.9}$$

Products of pure states are strictly separable.

Some examples of pure maximally entangled two-qubit states are conventional Bell

states [8]:

$$|\Psi^+\rangle = \frac{1}{\sqrt{2}}(|H\rangle \otimes |V\rangle + |V\rangle \otimes |H\rangle)$$

$$|\Psi^-\rangle = \frac{1}{\sqrt{2}}(|H\rangle \otimes |V\rangle - |V\rangle \otimes |H\rangle)$$

$$|\Phi^+\rangle = \frac{1}{\sqrt{2}}(|H\rangle \otimes |H\rangle + |V\rangle \otimes |V\rangle)$$

$$|\Phi^-\rangle = \frac{1}{\sqrt{2}}(|H\rangle \otimes |H\rangle - |V\rangle \otimes |V\rangle).$$

$$(1.10)$$

States can also posses degrees of entanglement. If we consider a parametrization of one of the conventional Bell states:

$$|\psi\rangle = \frac{1}{\sqrt{2}}(\cos\alpha|H\rangle \otimes |H\rangle + \sin\alpha|V\rangle \otimes |V\rangle), \tag{1.11}$$

then we can vary the amount of entanglement in the state by varying α. The state is maximally entangled for $\alpha = \frac{\pi}{4}$ and separable for $\alpha = \frac{n\pi}{2}$ where n is an integer.

1.4 Bell's Inequalities

1.4.1 CHSH Inequality

The Bell scenario, depicted in Fig. 1.2, has a source of entangled pairs of particles and two parties, Alice and Bob, who each get a particle from the entangled pair. The scenario is such that they each have two measurement settings to choose from independently of each other, and the result of the measurement they perform can be ± 1. We can define a parameter $E_{a,b}$ which is a measure of how correlated the measurement outcomes from Alice and Bob are based on the settings they chose (a or a' for Alice, b or b' for Bob):

$$E_{a,b} = \frac{N_{++} + N_{--} - N_{-+} - N_{+-}}{N_{++} + N_{--} + N_{-+} + N_{+-}}. \tag{1.12}$$

Where " $+$ " corresponds to a $+1$ measurement outcome, " $-$ " corresponds to a -1 measurement outcome and "N" refers to the number of coincidence counts for the specified
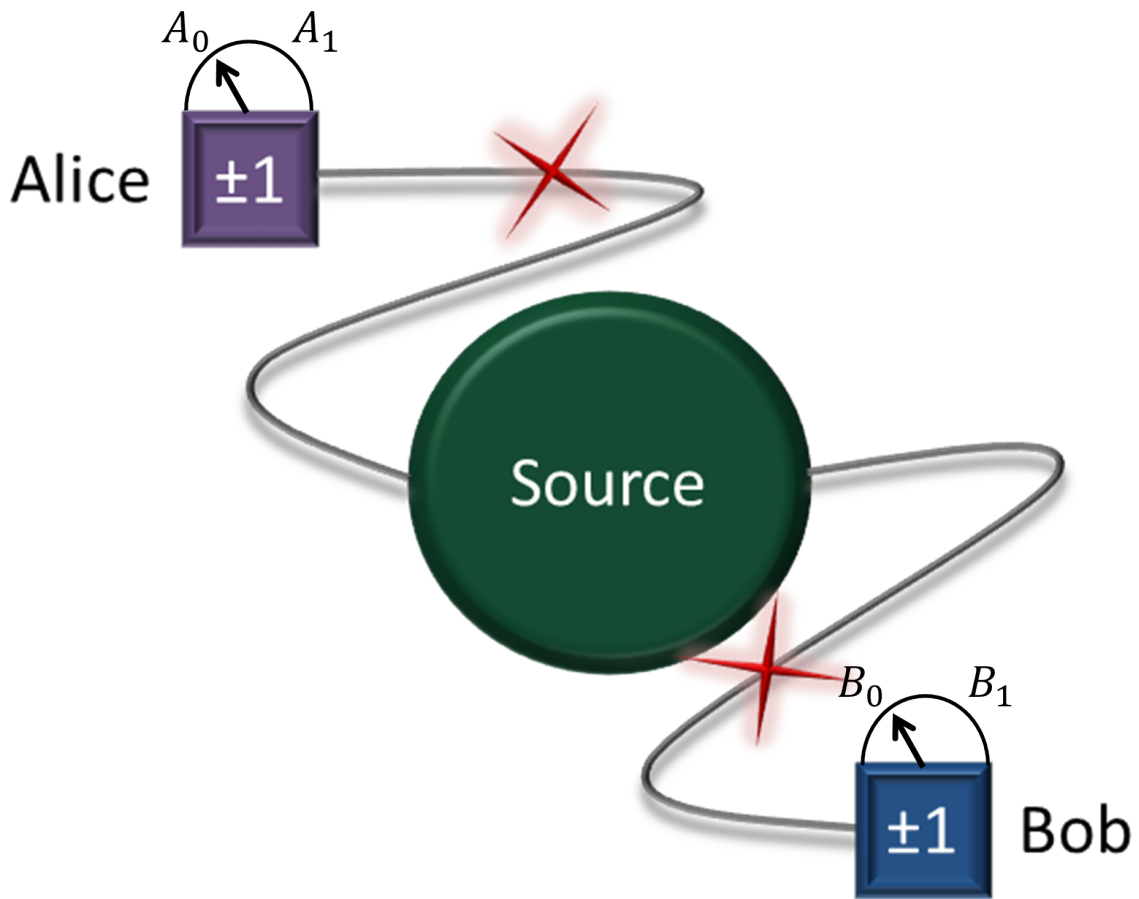
Figure 1.2: Representation of the Bell scenario depicted by the entangled photon source sending entangled photons to the two parties: Alice and Bob. The parties then have a choice of two measurement settings, and the result of their measurement will be ± 1.

measurement outcome. Clauser, Horne, Shimony and Holt (CHSH) published in their paper an inequality using these correlations, now called the CHSH inequality [11]:

$$|E_{a,b} + E_{a',b}| + |E_{a,b'} - E_{a',b'}| \leq 2. \tag{1.13}$$

This inequality holds for any Local Hidden Variable Model (LHVM) of physics. LHVMs were introduced to help explain quantum correlations in nature. It was thought that *local hidden variables* governed measurement results and that distant events could have no instant effects on, or correlation with, local events. This assumption lead to the CHSH inequality, which states that for LHVM to be true the maximum value of equation 1.14 must be 2. Entanglement is a quantum property that is nonlocal (it persists regardless of spatial separation) and therefore cannot be described by the LHVM, so violation of these inequalities that assume LHVM is often used to test for the presence of nonlocal properties such as the aforementioned entanglement.

1.4.2 The Generalized Bell Inequality

We can define a more general equation involving these correlations and equate it to the expectation value of the Bell parameter, $\langle Z \rangle$.

$$c_1 E_a + c_2 E_{a'} + c_3 E_b + c_4 E_{b'} + c_5 E_{a,b} + c_6 E_{a',b} + c_7 E_{a,b'} + c_8 E_{a',b'} \equiv \langle Z \rangle. \tag{1.14}$$

The coefficients c_i are real constants. This equation also incorporates single particle or "marginal" correlations, which are defined as:

$$E_a = \frac{N_{++} - N_{--} - N_{-+} + N_{+-}}{N_{++} + N_{--} + N_{-+} + N_{+-}}. \tag{1.15}$$

These single particle correlations sum the incidences where the measurement outcome for that particular setting was positive, regardless of what the measurement outcome from the other party in the experiment was.

Wolf and Yelin [12] postulated the existence of three new families of Bell inequalities by varying and parameterizing the values of the c_i coefficients. The upper bounds for the

three families are provided for both the LHVM and the quantum mechanical model. In order to recover the quantum mechanical bounds first we must define a set of operators: A_0, A_1, B_0, B_1, where A_0 and A_1 refer to the measurement operator on Alice's particle using setting a and a' respectively. Similarly, B_0 and B_1 correspond to the measurement operators for settings b and b' respectively on Bob's particle. With this in mind, Wolf and Yelin propose that we can parameterize these operators, considering only the difference in angle between each party's measurement settings. This causes no loss of generality, and by imposing a reflection symmetry, results in the following definitions [12]:

$$
\begin{aligned}
A_0 &\equiv [\cos(\theta_A)\sigma_x + \sin(\theta_A)\sigma_y] \otimes \mathbb{1} \otimes \mathbb{1}... \\
A_1 &\equiv [\cos(\theta_A)\sigma_x - \sin(\theta_A)\sigma_y] \otimes \mathbb{1} \otimes \mathbb{1}... \\
B_0 &\equiv \mathbb{1} \otimes [\cos(\theta_B)\sigma_x + \sin(\theta_B)\sigma_y] \otimes \mathbb{1}... \\
B_1 &\equiv \mathbb{1} \otimes [\cos(\theta_B)\sigma_x - \sin(\theta_B)\sigma_y] \otimes \mathbb{1}....
\end{aligned}
\tag{1.16}
$$

We can define Z in the operator notation as:

$$
Z \equiv c_1 A_0 + c_2 A_1 + c_3 B_0 + c_4 B_1 + c_5 A_0 \cdot B_0 + c_6 A_1 \cdot B_0 + c_7 A_0 \cdot B_1 + c_8 A_1 \cdot B_1, \tag{1.17}
$$

where the coefficients c_i are real constants. Finding the maximum value of $\langle Z \rangle$ given the above definitions can be rewritten as an eigenvalue problem in variables θ_A, θ_B. By solving for the characteristic equation of the eigenvalue problem and taking the largest root, we recover the maximum bounds for $\langle Z \rangle$ in the quantum limit given a set of $\{c_i\}$ [12].

1.4.3 Reducing to Three Families

If the values for $\{c_i\}$ are constrained to be: $c_i = -1, 0, 1$, then there are $3^8 = 6561$ possible combinations. In order to narrow this down to three families, some physical symmetries were utilized. First one could consider relabeling Alice and Bob: $A_i \leftrightarrows B_i$. There can be equivalent permutations of the measurement indices for each party: $A_0 \leftrightarrows A_1$, $B_0 \leftrightarrows B_1$. The last symmetry would be the definition of a "positive" and "negative" measurement: $A_i \leftrightarrows -A_i$, $B_i \leftrightarrows -B_i$. These symmetries reduce the collection to a set of 98 unique combinations. If this is then confined to only those combinations that exhibit a gap between the local hidden variable model and the no-signaling faster than light model, then this can be reduced to three families, each with a parameterized unique set of $\{c_i\}$ [12].

1.4.4 Volume Analysis

Wolfe and Yelin use *volume analysis* to quantify the size of the particle correlations in the various models they explore. This analysis sets the dimension of the correlation by considering the number of parties, measurement settings (or inputs) and possible outcomes. Combined with constraints imposed by the model being used (the CHSH inequality is a constraint example for the LHVM) this maps out the correlation volume for that model. For a complete description of this method see Ref. [13].

1.5 Envariance

Envariance is a quantum symmetry of nature present in entangled quantum states. The term "envariance" was first coined by W. Zurek to mean "environment assisted invariance" [14]. This symmetry of envariance has been used in a proof of Born's rule, operating under the ideas of decoherence [15].

1.5.1 Definition and Properties

The property of envariance can be defined in the following way:

$$U_{\mathsf{S}}|\psi_{\mathsf{SE}}\rangle \;=\; (u_{\mathsf{S}} \otimes \mathbb{1}_{\mathsf{E}})|\psi_{\mathsf{SE}}\rangle = |\eta_{\mathsf{SE}}\rangle \tag{1.18}$$

$$U_{\mathsf{E}}|\eta_{\mathsf{SE}}\rangle \;=\; (\mathbb{1}_{\mathsf{S}} \otimes u_{\mathsf{E}})|\eta_{\mathsf{SE}}\rangle = |\psi_{\mathsf{SE}}\rangle. \tag{1.19}$$

Where $|\psi_{\mathsf{SE}}\rangle$ is a pure entangled two-qubit quantum state where one qubit is represented by the environment "E" and the other is represented by the system "S". U_{S} is a unitary applied only to the system qubit and U_{E} is a unitary applied only to the environment qubit. The state $|\psi_{\mathsf{SE}}\rangle$ is envariant under the transformation U_{S} if Eqns. 1.19 and 1.20 hold, or if there exists a unitary U_{E} such that after the system unitary is applied, the original state can be recovered while only acting on the environment qubit with U_{E}. Envariance for a general U_{S} is a uniquely quantum property, always requiring entanglement [15].

1.6   Comparing Quantum States

In order to effectively measure and compare experimental quantum states, the state must be reconstructed from the results of projective measurements. In particular in order to calculate the fidelity of an experimental state with a theoretical one, the density matrix of the experimental state must be reconstructed. When performing the reconstruction process, it is assumed we have a large, but finite, number of identical quantum states to perform measurements on. The process of reconstructing a quantum state from these measurement results is called quantum state tomography [16].

1.6.1   Quantum State Tomography

One of the earliest methods of optical quantum state tomography was single qubit tomography, which measured the Stokes parameters to characterize polarization states [17]. There has been significant growth and development in this area in terms of methods and applicability to other physical systems [18, 19, 20]. The majority of these methods rely on directly inverting the linear equations developed from the experimental data. Using this linear inversion, we can write the reconstructed density matrix as [21]:

$$hat\rho = \sum_{\nu=1}^{16}[\sum_{\mu=1}^{16}(B^{-1})_{\nu,\mu}\hat{\Gamma}_{\mu}]n_{\nu}, \tag{1.20}$$

where n_{ν} refer to the measurement outcomes (number of coincidence counts when using the platform of single-photons) for the state $|\psi_{\nu}\rangle$, and $B_{\nu,\mu} = \langle\psi_{\nu}|\hat{\Gamma}_{\mu}|\psi_{\nu}\rangle$. Some benefits to this approach are that it is conceptually simple and easy to implement. Some drawbacks are that this can lead to an un-physical reconstructed state (recovering a density matrix with negative eigenvalues, or $Tr(\rho) \neq 1$). Another method, called the maximum likelihood method, applies the constraint that the state be physical and then recovers the most likely state that has been measured [16].

Maximum Likelihood Quantum State Tomography

Maximum likelihood, as previously stated, is a form of quantum state tomography which overcomes some of the issues present in the linear inversion method. Its mechanism is to constrain the reconstructed density matrix to be physical and recover the most likely state from the experimental data [16, 21]. In order to do this there must first be constraints placed on $\hat{\rho}$ such that it is guaranteed to be physical. First, parameterize $\hat{\rho}$ in terms of another square matrix $\hat{T}$:

$$\hat{\rho} = \frac{\hat{T}^\dagger \hat{T}}{Tr[\hat{T}^\dagger \hat{T}]}. \tag{1.21}$$

Because $\hat{T}$ is a square matrix and $\hat{T}^\dagger$ is the Hermitian conjugate of $\hat{T}$, $\hat{\rho}$ is guaranteed to be Hermitian and positive, and by dividing by the trace of $\hat{T}^\dagger \hat{T}$ it is also guaranteed to be normalized ($Tr[\hat{\rho}] = 1$). $\hat{T}$ now needs to be parameterized in such a way to reflect the parameters required by $\hat{\rho}$. For the two qubit case:

$$\hat{T} = \begin{pmatrix} t_1 & 0 & 0 & 0 \\ t_5 + it_6 & t_2 & 0 & 0 \\ t_{11} + it_{12} & t_7 + it_8 & t_3 & 0 \\ t_{15} + it_{16} & t_{13} + it_{14} & t_9 + it_{10} & t_4 \end{pmatrix}$$

. Here the t_i are the 16 parameters specifying $\hat{\rho}$ and $\{t_i\} \in \mathbb{R}$. In order to choose the most likely state there must be some measure of how close the agreement is between the experimental data and the reconstructed state. This can be defined using a probability measure [21]:

$$P(n_1, n_2 ... n_l) = \frac{1}{\tilde{N}} \prod_{\nu=1}^{l} \exp\left(-\frac{(\tilde{n}_\nu - n_\nu)^2}{2\tilde{n}_\nu}\right), \tag{1.22}$$

where $\tilde{n}_\nu = N\langle\psi_\nu|\hat{\rho}|\psi_\nu\rangle$ refers to a prediction of the average counts for a given measurement (the N comes from known parameters such as the flux in the experiment). This allows the presentation of the probability above, which is a Gaussian distribution centred about $\tilde{n}_\nu$. (We choose a Gaussian distribution as it is a good approximation for a Poissonian distribution with a large mean, and our errors model a Poissonian distribution.) The set $\{n_l\}$ refers to the set of l actual count measurements, and $\tilde{N}$ is a normalization constant.

To find the most likely state, the function must be maximized over all the parameters from $\hat{T}$, $\{t_i\}$. In practice it is simpler to work with the logarithm of the function, rewriting the problem as a minimization of this function over the $\{t_i\}$ parameters[21]:

$$L(t_1, t_2...t_i) = \sum_{\nu=1}^{l} \left(\frac{(N\langle\psi_\nu|\hat{\rho}|\psi_\nu\rangle - n_\nu)^2}{2N\langle\psi_\nu|\hat{\rho}|\psi_\nu\rangle} \right). \tag{1.23}$$

It should be noted that there are no constraints on the maximum value of l with regards to the dimension of the state (unlike linear inversion which results in an over-constrained density matrix if the number of measurements exceed the square of the state dimension). This allows for there to be an over-complete set of experimental measurements (for two-qubits this is a set greater than the 16 required measurements). So in conclusion, this method guarantees a physical state is reconstructed and allows for a larger set of measurements to be used in determining that state [16, 21]. All the experiments described in this thesis used an over-complete set of 36 measurements corresponding to the eigenstates $\sigma_i \otimes \sigma_j$ where i, j are x, y, z. The maximum likelihood method was used for state reconstruction.

1.6.2   Quantum Fidelity

Quantum fidelity is a distance measure between quantum states, used as a way of determining how close the two states are. In density matrix format its is defined as [2]:

$$F(\rho, \sigma) = \{\text{Tr}[(\sqrt{\rho}\sigma\sqrt{\rho})^{1/2}]\}^2, \tag{1.24}$$

where ρ and σ represent the density matrices of the states being compared. For a set of pure states where $\rho = |\psi\rangle\langle\psi|$ and $\sigma = |\phi\rangle\langle\phi|$ we have:

$$F(\rho, \sigma) = |\langle\phi|\psi\rangle|^2. \tag{1.25}$$

From this definition we have if $\rho = \sigma$ then $F(\rho, \sigma) = 1$, and if ρ is orthogonal to σ then $F(\rho, \sigma) = 0$.

1.7 Creating Entangled Photon States

Experimental quantum optics is a platform for quantum computing that relies on the interaction and detection of single-photons. The implementation for strictly linear quantum optics in quantum computing was presented as a viable scheme in 2001 [6] and the first high intensity polarization entangled sources were developed by Paul Kwiat and colleagues in the 1990's [22, 23]. For the purposes of this thesis we will be restricted to working with the polarization degree of freedom of the photons, and creation of our entangled pairs will be achieved through an optical nonlinear process called spontaneous parametric down-conversion.

1.7.1 Spontaneous Parametric Down-Conversion

Spontaneous parametric down-conversion (SPDC) is currently the most commonly used way to produce pairs of entangled photons. It occurs through laser pumping a nonlinear crystal. Pairs of correlated photons (the "signal" and the "idler") of higher wavelength than the pump are released. This is a strictly quantum effect and does not occur in the regime of classical nonlinear optics.

To derive this effect, first consider the electric fields involved:

$$\hat{E_p^{(+)}} = E_0 \exp[i(k_p z - \omega_p t)]. \tag{1.26}$$

This is a monochromatic classical wave traveling in the $\hat{z}$ direction which describes the electric field of the pump laser. This is an acceptable approximation for our laser as the pump is assumed to be intense and undergoes negligible depletion. The fields for the signal and idler must follow the convention for the quantized electromagnetic field as they represent the electric field of single-photons:

$$\hat{E_n^{(-)}} = -i\sqrt{\frac{\hbar \omega_n}{2\epsilon_0 V}} \hat{a_n^\dagger} \exp[-i(k_n z - \omega_n t)], \tag{1.27}$$

14

where $n = s, i$ for the signal and the idler, $\hat{a}_n^\dagger$ is the creation operator, and again we have assumed linear propagation in the $\hat{z}$ direction. Additionally, we are only considering one output mode, otherwise there would be a sum over the output modes. For a more general description of the SPDC process see Ref. [24].

To find the Hamiltonian for this process we start with the electric field density for a classical field in a nonlinear medium and then quantize the electromagnetic field [24, 25]:

$$\hat{H} = \epsilon_0 \int_V d^3 r \chi^{(2)} \hat{E}_p^{(+)} \hat{E}_s^{(-)} \hat{E}_i^{(-)} + h.c.. \tag{1.28}$$

To determine the state resulting from applying this Hamiltonian we need to consider the time evolution of a quantum state starting from vacuum, where $|\psi(0)\rangle$ is the vacuum state:

$$|\psi(t)\rangle = \exp\left[\frac{1}{i\hbar} \int_0^t dt' \hat{H}(t')\right] |\psi(0)\rangle \tag{1.29}$$

If we consider only first order perturbative terms after expanding the exponential in a Taylor series the result is:

$$|\psi(t)\rangle = |\psi(0)\rangle + \frac{1}{i\hbar} \int_0^t dt' \hat{H}(t')|\psi(0)\rangle. \tag{1.30}$$

Now combining our definitions for the Hamiltonian and the electric fields and neglecting the quantum output of the pump we recover:

$$|\psi(t)\rangle \sim \frac{-1}{i\hbar} \epsilon_0 E_0 \int_0^t dt' \int_V d^3 r \chi^{(2)} \sqrt{\frac{\hbar\omega_s}{2\epsilon_0 V}} \sqrt{\frac{\hbar\omega_i}{2\epsilon_0 V}} \hat{a}_s^\dagger \hat{a}_i^\dagger$$
$$\exp[i(k_p - k_s - k_i)z] \exp[i(\omega_s + \omega_i - \omega_p)t]|\psi(0)\rangle. \tag{1.31}$$

Because of the plane wave assumption the only nontrivial part of the volume integral is over the $\hat{z}$ direction. For simplicity we assume that the second order nonlinear susceptibility $(\chi^{(2)})$ is independent of z. This is not true for periodically poled materials, the type of which were used in the two experiments in this thesis, but this correction to the final output state will be dealt with in the next section on quasi-phase matching. After a few

15

simplifications, including a sufficiently lengthy interaction time t, and ignoring the output in the vacuum state we recover:

$$|\psi(t)\rangle \sim \frac{iE_0}{2}\sqrt{\omega_s\omega_i}\chi^{(2)}\delta(\frac{\Delta\omega}{2})\mathrm{sinc}(\frac{\Delta k L_z}{2})\exp[\frac{-i}{2}(\Delta\omega t - \Delta k L_z)]|1\rangle_s|1\rangle_i. \qquad (1.32)$$

Where $\Delta\omega = \omega_p - \omega_s - \omega_i$, $\Delta k = k_p - k_s - k_i$ and L_z is the length of the crystal. This result indicates that the output from this nonlinear process is always a pair of signal and idler photons, and because of the delta function, only occurs when $\omega_p = \omega_s + \omega_i$ (when $\delta \neq 0$). This is a statement of energy conservation and is also why sometimes SPDC is referred to as "photon splitting". In order to maximize the efficiency of the process the $\mathrm{sinc}(\frac{\Delta k L_z}{2})$ term needs to be maximized. This is done through the process of phase matching which will be discussed in the next section.

There are three types of SPDC and the main differences are the polarizations of the output pair of photons. The crystal used in both experiments was a type II crystal which gives a horizontally polarized signal and a vertically polarized idler. This relation of perpendicular polarizations, guaranteed in each pair of photons produced by SPDC, is part of what makes entanglement in a Sagnac source possible.

1.7.2 Phase Matching and Quasi-Phase Matching

As stated previously, in order to facilitate the most efficient SPDC process the $\mathrm{sinc}(\frac{\Delta k L_z}{2})$ term needs to be maximized. The phase matching condition for this situation is $k_p = k_s + k_i$. Meeting this condition means that the signal and idler photons are created in phase with the pump, giving the best efficiency for the process. For bulk crystals tuning the angle of the input beam in relation to the crystal axis will complete the phase matching condition, but will hurt the efficiency of the process as this causes issues with walk-off, limiting the length of the crystal. For ferromagnetic materials such as potassium titanyl phosphate (KTP) and lithium niobate (LN) there is an alternative approach to this technique called quasi-phase matching.

Quasi-phase matching was first proposed along with several other phase matching schemes in 1962 [26]. A more recent and thorough review of the subject can be found in Ref. [27]. Quasi-phase matching is a fabrication technique usable on ferromagnetic crystals which causes the birefringent layers in the crystal to be inverted over a specified length known as the *poling period*. These oppositely oriented birefringent layers can be thought of as defining the nonlinear permittivity as a square wave in the $\hat{z}$ direction (recall earlier we made the assumption that the electric permittivity $\chi^{(2)}$ was independent of z, this will now be corrected):

$$\chi^{(2)}(z) = \chi_0^{(2)}\text{sign}[\cos(\frac{2\pi z}{\Lambda})], \tag{1.33}$$

where $\chi_0^{(2)}$ is the nonlinear permittivity of the material, z is the position in the crystal, and Λ is the poling period. Because of the nature of the Sign function we can rewrite $\chi^{(2)}(z)$ as a Fourier series:

$$\chi^{(2)}(z) = \sum_{n=-\infty}^{\infty} A_m \exp(ik_n z). \tag{1.34}$$

By integrating and solving for the A_m coefficients we recover:

$$\chi^{(2)}(z) \approx \sum_{n=-\infty}^{\infty} \frac{2\chi_0^{(2)}}{\pi n} \sin(\frac{\pi n}{2}) \exp(\frac{i2\pi nz}{\Lambda}). \tag{1.35}$$

We only need one of the terms in this series to be large in order to meet the phase matching condition, and the choice that will provide the largest term is $n = \pm 1$. Then we are left with:

$$\chi^{(2)}(z) = \frac{2}{\pi}\chi_0^{(2)} \exp(\frac{\pm i2\pi z}{\Lambda}). \tag{1.36}$$

If we insert this z dependent nonlinear permittivity into our integral for the final output state we get:

$$|\psi t\rangle \sim \frac{-1}{i\hbar}\epsilon_0 E_0 \int_0^t dt' \int_V d^3 r \frac{2}{\pi}\chi_0^{(2)} \exp(\frac{\pm i2\pi z}{\Lambda})\sqrt{\frac{\hbar\omega_s}{2\epsilon_0 V}} \sqrt{\frac{\hbar\omega_i}{2\epsilon_0 V}}\hat{a}_s^\dagger \hat{a}_i^\dagger$$
$$\exp[i(k_p - k_s - k_i)z] \exp[i(\omega_s + \omega_i - \omega_p)t]|\psi(0)\rangle. \tag{1.37}$$

Completing the integrals as before and simplifying, the final output state can be written as:

$$|\psi(t)\rangle \sim \frac{iE_0}{2}\sqrt{\omega_s\omega_i}\frac{2}{\pi}\chi_0^{(2)}\delta(\frac{\Delta\omega}{2})\text{sinc}[\frac{(\Delta k \pm \frac{2\pi}{\Lambda})L_z}{2}] \exp[\frac{-i}{2}(\Delta\omega t - \Delta k L_z)]|1\rangle_s|1\rangle_i. \tag{1.38}$$

17

This means that our phase matching condition changes to:

$$k_p = k_s + k_i \mp \frac{2\pi}{\Lambda}. \tag{1.39}$$

By tuning the poling period Λ, the extra term in the phase matching equation changes, effectively meeting the phase matching condition.

It is often desirable to have the signal and idler degenerate (have the same wavelength) as this makes them indistinguishable and enhances the efficiency of the down-conversion process. It is essential in the Sagnac geometry to have degenerate pairs to create entanglement. Consequently, it is usually required to tune the output photons to the desired wavelength and still meet the phase matching conditions. It can be difficult to do this solely with quasi-phase matching as fabrication techniques limit the accuracy and tolerance of Λ. There is a technique called temperature tuning which can fine tune the phase matching condition. The index of refraction of the nonlinear material is temperature dependent and thus Δk is also temperature dependant based on our earlier definition. This works very well in conjunction with quasi-phase matching as it is not able to make large changes to the phase matching, but can fine tune the wavelengths of the output photons if the basic phase matching condition is already met. This is done by placing the crystal in a oven, and changing the temperature.

1.7.3   Implementing Unitaries on Single-Photons

Unitary transformations can be described as rotations about a chosen axis. In optics the chosen method for rotating the polarization of a beam of light, or in our case a photon, is to use wave plates. A zero-order wave plate (the type used in our experiments) consists of a thin crystal plate with a very specific thickness, designed to perform a very specific phase shift on incoming light. A half wave plate (HWP) rotates the light polarization by 180° about an axis set at an angle θ from the horizontal axis, in the real plane [28]:

$$U_{HWP}(\theta) = \exp\left[\frac{i\pi}{2}\right] \begin{pmatrix} \cos(2\theta) & \sin(2\theta) \\ \sin(2\theta) & -\cos(2\theta) \end{pmatrix}. \tag{1.40}$$

It is worth noting that the angle θ, which is changed by rotating the wave plate, is a physical angle and must encode the fact that horizontal and vertical polarizations are only $90°$ apart, as they represent the orthogonal plane waves of the electromagnetic field. For example, to take a beam from being horizontally polarized to vertically polarized the HWP must be set at $45°$. This puts the axis of rotation at diagonal, halfway between horizontal and vertical, which is $90°$ on the Bloch sphere. Quarter wave plates (QWP) operate in much the same way, but their rotation about the chosen axis is $90°$ instead of the $180°$ for the HWP:

$$U_{QWP}(\theta) = \frac{1}{\sqrt{2}} \begin{pmatrix} 1 + i\cos(2\theta) & i\sin(2\theta) \\ i\sin(2\theta) & 1 - i\cos(2\theta) \end{pmatrix}. \tag{1.41}$$

See Table 4.1 for the wave plate settings used in the envariance experiment.

Chapter 2

The Entangled Photon Source

2.1 Introduction

A Sagnac source of polarization entangled photon pairs was central to both experiments reported in this thesis. The present chapter includes more details on the experimental setup of the source and a discussion of alignment methods and troubleshooting techniques.

2.2 Experimental Setup

The name for the Sagnac source comes from the Sagnac interferometer, which is an interferometer with counter-prorogating paths on a closed loop. There have been several examples of different configurations for the Sagnac source over the last few years [29, 30, 31, 32, 33]. The design for the Sagnac used in our experiments (see Fig. 2.1) is based on the designs shown in Refs. [31, 32] and it follows closely to the setup outlined in [34]. This set-up configuration was used in both experiments save for the placement of the quarter wave plate, which will be discussed later. For the set-up in Fig. 2.1, the laser is a Toptica iWave continuous wave diode laser at 404.5 nm. First the laser passes through an optical isolator to prevent reflected light from passing back into the laser, and is directed via mirrors to the first half wave plate (HWP). This wave plate sets the incoming polarization for the
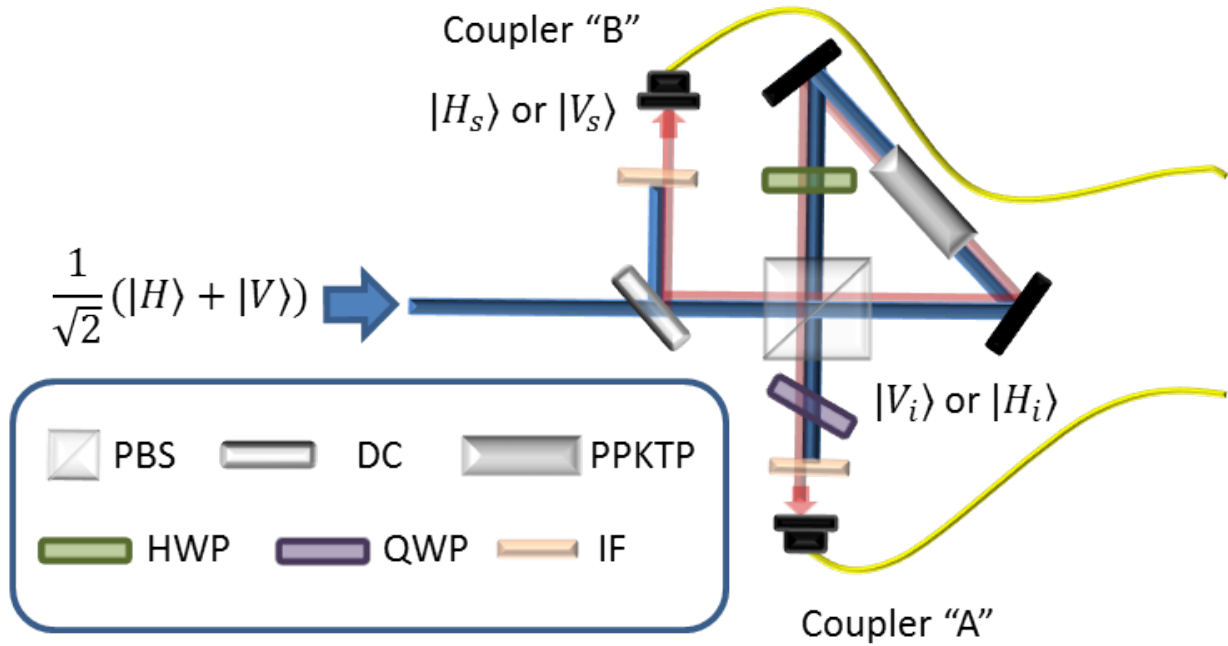
Figure 2.1: Sagnac source setup. Diagonally polarized 404.5 nm light is pumped through the lens, traveling in superposition through the two paths created by the polarizing beam splitter (PBS). The horizontal photons follow the transmitted (counterclockwise) path, generating pairs of horizontal idler and vertical signal photons (through type II SPDC). The vertical photons follow the reflected (clockwise) path also generating pairs of horizontal idler and vertical signal photons (the vertical pump photons are transformed to horizontal by the HWP in the triangle to satisfy the phase matching in the crystal). As the two paths are indistinguishable, pumping with an equal coherent superposition of horizontal and vertical will create an entangled state.

source. The light passes through a lens (focal length 200 mm) to focus it onto the crystal, and a dichroic mirror which at 45° transmits blue light and reflects red. The beam then reaches the polarizing beam splitter (PBS). The PBS creates two indistinguishable paths around the Sagnac triangle. This consists of two mirrors (which form the corners of the triangle) and a nonlinear crystal (which sits in the centre of the hypotenuse of the Sagnac triangle). The crystal is a periodically poled potassium-titanyl-phosphate (PPKTP) crystal, 10 mm long and heated at 75° to complete the phase matching. Through the process of spontaneous parametric down-conversion (SPDC) two photons at 808 nm, the signal and the idler, are emitted from the pump photons. The crystal is set for type II phase matching so the signal photon is horizontally polarized and the idler photon is vertically polarized. In this geometry, incoming horizontal light will pass through the PBS and be reflected counterclockwise around the triangle, creating the pair of 808 nm signal and idler photons. The two photons pass through the HWP inside the Sagnac triangle which is set at 45°, switching their polarizations to a vertical signal and a horizontal idler. At the PBS the vertical signal photon is reflected to the dichroic mirror, and again reflected. It passes through a low pass filter to coupler "B". The horizontal idler photon passes through a QWP (this is tilted to set the phase of the state) and a low pass filter to coupler "A". Incoming vertically polarized light will be reflected clockwise on the PBS around the Sagnac triangle. It will pass through the triangle HWP before the crystal, changing its polarization to horizontal. It then down-converts in the crystal producing a horizontal signal photon, which travels through the PBS to be reflected by the dichroic mirror to coupler "B", and a vertical idler photon which is reflected at the PBS through the phase setting QWP and the filters to coupler "A". Thus the state produced is:

$$|\psi\rangle = |H_i\rangle|V_s\rangle + e^{i\phi}|V_i\rangle|H_s\rangle. \tag{2.1}$$

The phase can be adjusted by tilting the quarter wave plate to give two of the four Bell states. The other two can be attained by the use of polarization controls in the fibre after the source.

2.2.1   QWP Placement

The set-up for this source was done according to the instructions for the setup of a Sagnac source outlined in Ref. [34]. The only deviation from this in the setup itself was the placement of the QWP. In Ref. [34] the QWP is placed directly after the HWP that sets the pump polarization, whereas in the setup for the second experiment in this thesis, the QWP is placed directly in front of the filter for coupler "A". This alteration was made because the original placement caused the beam heading into the Sagnac triangle to be translated slightly when significant tilt changes were made to the QWP. As the Sagnac triangle is significantly more challenging to align than the couplers, the QWP was moved so only the coupler would have to be adjusted when significant tilt changes were made to the QWP. This becomes particularly useful when switching between different Bell states, and more easily facilitates creating high fidelity states.

2.2.2   Notes on Back-Reflection

As stated in Ref. [34], every element in the source should be back-reflected as far back to the pump laser as possible when first aligned. So the reflection off the element in question should be aligned to the path of the laser beam, using an iris as far back along the laser path as possible. Certain key elements such as the lens, the crystal and the beam splitter require very precise back-reflection, or the source will not produce a high quality entangled state. Another advantage to careful back-reflection is it can be used to replace single elements in the source without complete realignment. Methods for this are outlined in the appendix.

2.3   Alignment Methods

Choosing an alignment method is a bit like choosing appropriate footwear, context is everything. In this section two different methods of alignment will be discussed within their appropriate contexts. The first is outlined in Ref. [34], and the other is a newly developed method. These methods target the *Sagnac triangle* as shown in Fig. 2.2
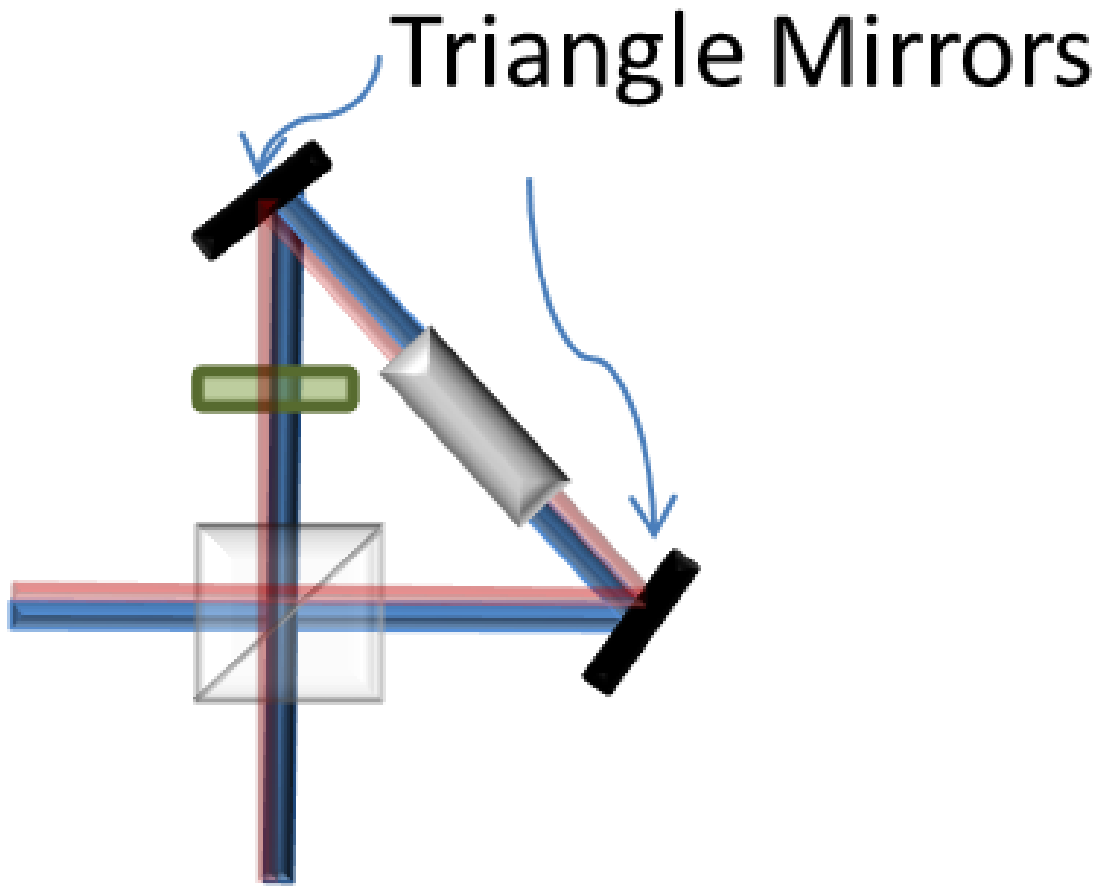
Figure 2.2: Sagnac source triangle. The two black rectangles denote the *triangle mirrors* referred to later in the alignment methods.

2.3.1 The "Hiking Boot" Method

This method is outlined in detail in Ref. [34], and a step-by-step procedure is also provided in this section. The main attribute of this method is that, provided the key elements are correctly placed, it will always be successful in aligning the Sagnac. For very unaligned triangle mirrors several iterations may be required, but with each iteration it will move closer and closer to alignment (there is a caveat to this when approaching perfect alignment. One of the main drawbacks is it is slow. One iteration can take from 15 min to an hour to perform and often multiple iterations are required. Another issue is that if the starting alignment is very good, this method can make it a little worse, making it very difficult to use it to maintain a very precise alignment. This method however, is very straightforward and effective, particularly when the setup is very misaligned. This method is designed to align the Sagnac triangle [34]:

- Set the first HWP so that the pump polarization is horizontal. Adjust the translations and tilts of the couplers to maximize the singles (or single counts, as opposed to coincident pairs) for each arm. Record the micrometer readings for all the translation stages.

- Set the first HWP so that the pump polarization is vertical. Adjust the TRANS-LATIONS ONLY of the couplers to maximize the singles for each arm. Record the micrometer readings for all the translation stages.

- Calculate the midpoint between the two positions and set all the translation stages to this point.

- Set the first HWP so that the pump polarization is diagonal. Adjust the the tilts of the triangle mirrors such that the total coincidences are maximized.

If the triangle mirrors are significantly misaligned then this process may need to be iterated several times to achieve the best results (so in other words: rinse and repeat). Significant improvement should be noticed with each iteration to the point of maximum alignment.

2.3.2 The "Stiletto" Method

The main attributes for this method are that it is fast and can produce very good results. One can usually perform multiple iterations in under 15 min, and it can take an already very well aligned setup and improve it. So when this method works, it works very well. The only problem with this comes if the starting setup is not already somewhat aligned. In this case successive iterations of this method can actually take the setup towards even greater misalignment. This makes it undesirable for first time alignment especially. Additionally, although being faster to implement it can also be more difficult to implement well. That being said it is a great candidate for regular maintenance when the technique is perfected, and usually produces a higher fidelity result than the other alignment method. Requirements for effective use of this method are that the triangle mirrors are already aligned to a certain degree. A good rule of thumb is if it has been aligned in the last few weeks, the stiletto method will probably work just fine. If it has been months since the last alignment, it is being realigned after being significantly disturbed, or it is the first fine alignment, it is best to use the hiking boot. The procedure for the stiletto method is as follows:

- Set the first HWP so that the pump polarization is horizontal. Note the number of coincidences between the vertical signal and the horizontal idler.

- Set the first HWP so that the pump polarization is vertical. Note the number of coincidences between the vertical idler and the horizontal signal.

- Whichever pump polarization resulted in the lower number of coincidences, set the pump to that polarization. Adjusting the translations only, attempt to bring the coincidences of this direction to the number of coincidences in the other direction.

- Set the pump polarization to the opposite. One of two things will have happened: either the previous step will have caused coincidences from both paths to increase, or the previous step will have increased the coincidences in one direction but not the other. If the former is true, then it is safe to attempt maximizing coincidences in this pump polarization using translations. Frequently return to the opposite polarization

to check that coincidences are increasing together. If this continues to be the case it is safe to adjust the tilts as well, still switching back and forth between the two pump polarizations. If increasing the coincidences in one path decreased them in the other, then the two paths are not perfectly superimposed. Using translation only, attempt to equate the coincidences in both paths. A good rule of thumb is to always work from the path with the lower coincidences and bring it halfway between its current number and the number that the other path currently has. Usually this will manifest itself in one degree of freedom more so than the other (i.e. vertical translation or horizontal translation). It is good to note which direction shows the most problems with path overlap as that direction will need more significant adjustments from the mirrors.

- Once the couplers are set, adjust the first HWP so that the pump polarization is diagonal. This should allow for a superposition of both paths. Adjust the triangle mirrors starting with the tilt direction that caused the most problems in the previous steps. Adjust the mirror tilts such that it maximizes the total number of coincidences. For the horizontal tilts do this by walking the two mirrors in the same direction; for the vertical tilts do this by walking the two mirrors in the opposite direction.

- If in the previous steps the coincidences for each path did not increase together repeat the procedure until this is the case. There should be progress made with each iteration to this point. If that is not the case the setup may not be aligned well enough to effectively implement this method, or there may be other problems with the source. we expect coupling efficiency of $\sim 20\%$ (ratio of singles to coincidences) when the source is optimally coupled.

2.4 General techniques for achieving high fidelity Bell states

Producing a high fidelity ($\sim 99\%$) Bell state from a Sagnac source depends first on the alignment and second on the various parameters of the measurement process. For the

alignment, what is most important is how it was originally set up, and what procedure is being used to maintain it. The setting of the parameters strongly depends on the goals of the individual experiment. Some general guidelines are included here for how to optimize the three main parameters under various scenarios: laser power, coincidence window and counting time.

2.4.1 Set-up and Maintenance

Step-by-step instructions for correct setup of a Sagnac source are outlined in Ref. [34]. In order to achieve the best quality states with the highest count rates, it is strongly recommended to follow the instructions in Ref. [34] to the letter. The only exception being the placement of the QWP which controls the phase of the output state. This should be placed in one of the outgoing arms, as recommended earlier for the best possible results. Maintaining a high fidelity Bell state can be difficult if this is not done, and also switching to a different Bell state will wreck the alignment. This is because if large changes are made to the tilt in the QWP (required for some state changes) then the beam will be translated.

Once the setup is initially aligned it will need to be fine tuned and maintained. After reaching a lower threshold alignment using the *hiking boot method* (recommended fidelity of at least 85%), the *Stiletto method* can be used to fine tune and maintain the alignment. This method can be used on a daily basis to produce the best possible results. Other components that should be checked and adjusted daily are the polarization controllers and the phase setting QWP. In our case the tilt of the QWP was the most unstable component and had to be set moments before taking data to achieve the best results. If the remaining components are securely mounted they shouldn't require adjustment for months at a time.

2.4.2 Laser Settings

Laser power settings are usually set to meet the required count rates of the experiment, with the consideration that if the power gets too high double pair emissions start to take place. Double pair emission is an effect of SPDC whereby instead of emitting one correlated pair of
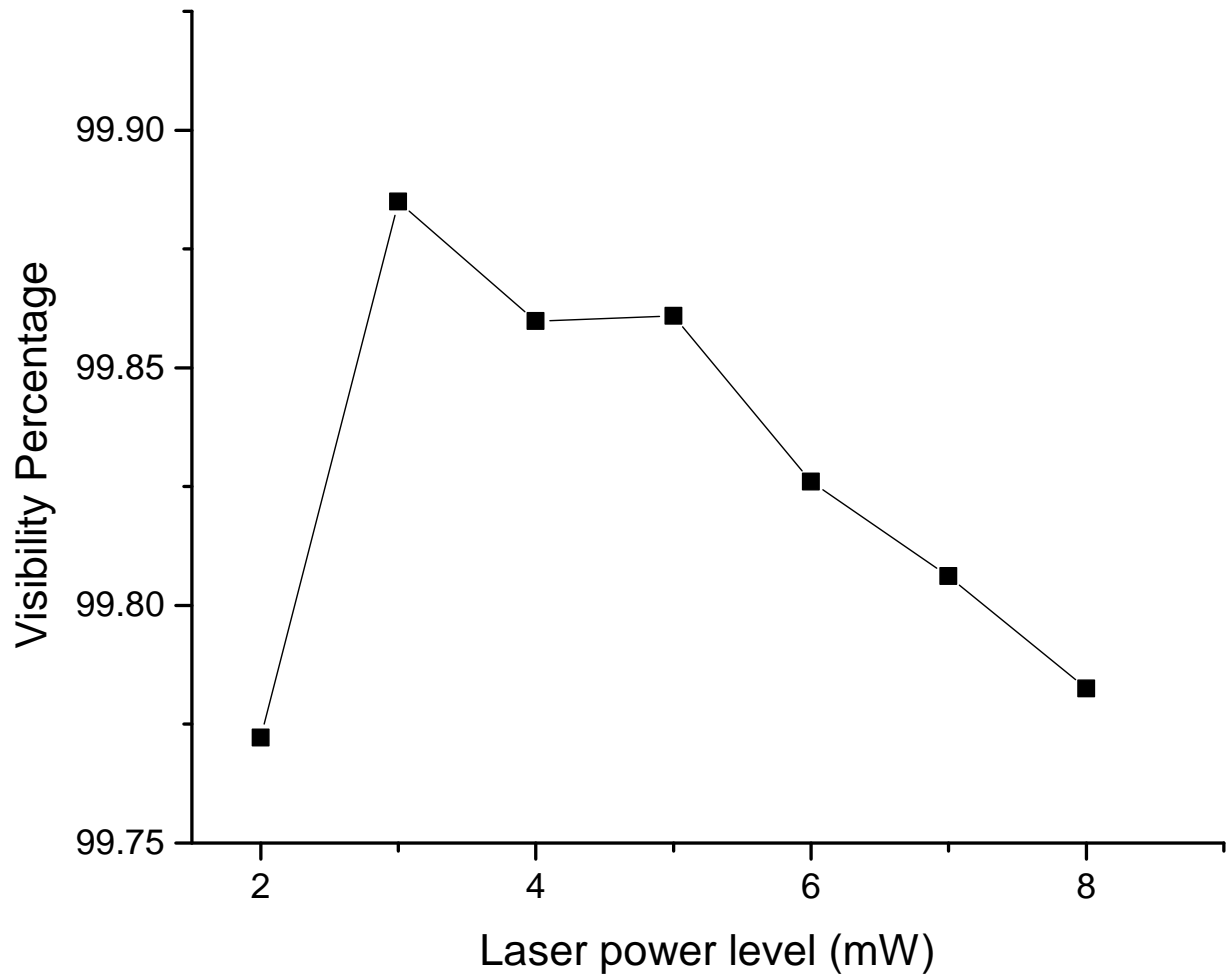
Figure 2.3: Measured visibility as a function of laser power. Here we compare the percent visibility of the state in the horizontal/vertical basis measured at different laser power levels to track the detrimental effects of double pair emissions..

photons, two pairs of correlated photons are emitted simultaneously. The effects of double pair emission can be seen in the visibility of a maximally entangled state. By comparing the visibility of the state over a range of powers we found that the optimal visibility given the performance of the laser at low power, was at 3 mW as is shown in Fig. 2.3; however, we opted for a power level of 6 mW to satisfy other experimental considerations. In general,aside from laser issues, reducing power will increase the visibility until accidental coincidences start to dominate, then the visibility will drop. The difference in visibility between 3 and 6 mW was 0.06%, so the effect on the final results was acceptably small. If the primary goal is the highest fidelity possible, then lower power is better.

2.4.3 Coincidence Window

The coincidence window is a (variable) parameter which limits the time lapse between two detection events for them to be considered as "coincident", i.e., "detected at the same time". This is important because photon pairs are created at the same time, and should therefore be measured coincidentally after they are spatially separated. A tighter coincidence window cuts down on the background, but if it is too tight many counts can be lost. One method to optimize it is to tighten the window until the measured coincidences start to drop. A very tight coincidence window can be problematic because once it goes below the detector jitter than there is no benefit for signal-to-noise and it just decreases coincidences. The best results were obtained when the alignment and phase setting were performed with a 3 ns window, and measuring and taking data was done with a 1 ns window. Changing this setting from 3 to 1 ns was enough to boost the state fidelity from 98% to 99%. This improvement is apparent when comparing the visibility of the two cases as shown in Table 2.1.

2.4.4 Counting Time

The counting time for each measurement is one of the parameters most affected by experiment-specific requirements. In our envariance experiment (chapter four) we limited our count time to 5 s to limit the effects of phase and polarization fluctuations in our experimental
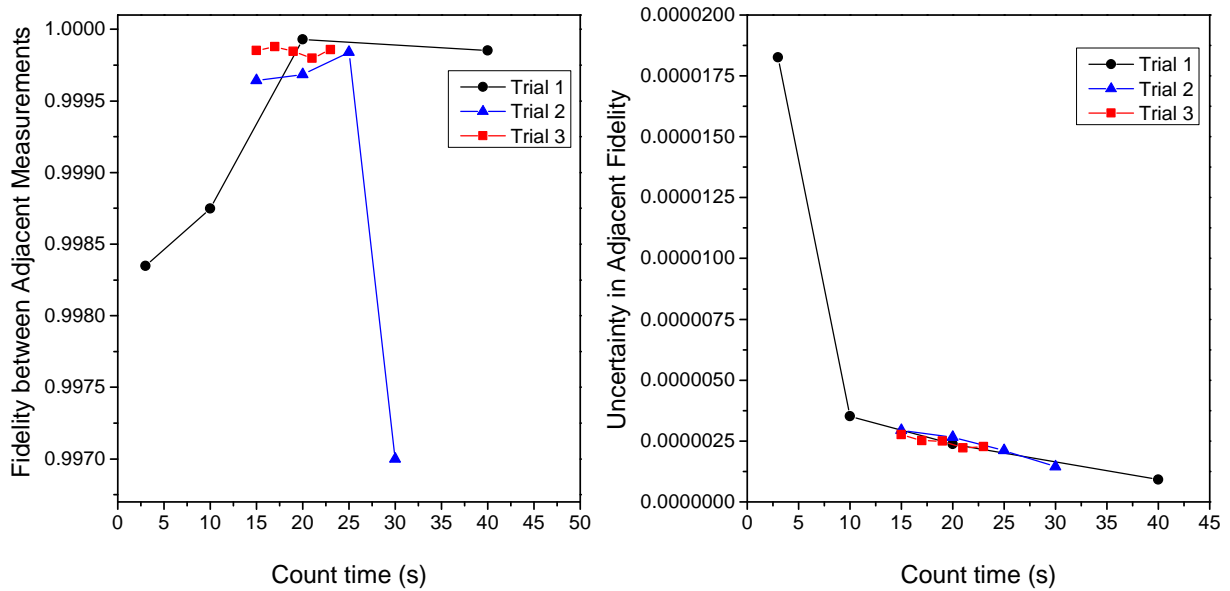
Figure 2.4: State fidelity and uncertainty as a function of measurement count time. For three different trials we show the fidelity of adjacent state measurements and the uncertainty in that fidelity for different measurement count times. Trial 1 tested the widest range of count times and subsequent trials tested increasingly narrower ranges of count times. Trial 1 shows a nonlinear relationship between uncertainty in the fidelity and count time (this is to be expected as this uncertainty was calculated using a Poissonian distribution). Trials 1 and 2 show that although increasing the count time continues to decrease the uncertainty it doesn't necessarily increase the fidelity (we believe this is due to drift in the source during the measurement process). Trials 2 and 3 indicate that the count range between 15 and 25 seconds produces the most consistent results in the fidelity.

31

Basis	3 ns Coinc. Window	1 ns Coinc. Window
H, V	98.4%	99.5%
D, A	98.2%	99.1%
R, L	98.8%	99.1%

Table 2.1: Percent visibility for different coincidence windows. Here we show the percent visibility for three different basis measurements with two different coincidence windows.

setup over time. However, we did several tests of how to achieve the highest fidelity between adjacent measurements by adjusting the count time of the measurements. Fig. 2.4 shows the results of three different trials comparing adjacent fidelity measurements and their uncertainty with measurement count time. We found the most consistent results at a measurement count time of ~ 20 s. This length provided consistent fidelities and good statistics (low uncertainty) for the state. Significantly longer times led to stability issues, and significantly shorter times led to higher uncertainty, and therefore impacted the fidelities between adjacent states. Unfortunately, although we made extensive attempts to run the experiment for longer count times ($15 - 20$ s), our best results overall came from a shorter count time (5 s) because of the dominating issues with source drift over the length of the experiment.

2.5   Trouble-shooting a Sagnac Source

Even following the previously suggested procedure for maintenance sometimes optics can be knocked or bumped. When its unclear which component is misaligned there is definitely a preferred order to try to fix things. This often happens at the least opportune times and can mean the entire setup requires realignment. There is a way to do a lot of replacement fixes without complete realignment, and it involves making use of the other back-reflected components. This procedure is outlined in the appendix and can save tremendous amounts of time, but only works as well as the other elements are back-reflected. It also becomes more and more challenging depending on how many elements are tampered with while trying to find the problem. This is why a preferred order to adjusting optics is important.

The safest order for trouble-shooting is a bit like medical procedure: start with the least invasive options.

2.5.1   Initial Inspection

A good cursory look at the setup before trying any alignment options is always a good idea. If one of the mounting elements has been broken or displaced it is usually visually apparent just from following the line of the laser path. If there is something broken or out of place that goes unnoticed, subsequent attempts to align the source will result in further misalignment and make it very difficult to realign the broken or out of place element (see the appendix for details on procedures for replacing broken items). So after taking a very close look at all the elements to see if anything is obviously misaligned then try one of the alignment methods (if "stiletto" doesn't provide results try the "hiking boot"). If it is clear that the problem still lies in the source and not in whatever analyzer or setup is connected to the source, then follow the sections bellow checking items depending on what the symptoms of the problem are. Most of the items listed aim to trouble-shoot low counts and/or low fidelity.

2.5.2   Spectral Filters

The filters are almost at the very end of the path so adjusting them only affects the coupler alignment. If they are not properly back-reflected this can really hurt the measured count rates. The reason for this is that filters are usually designed to operate with the incoming beam at normal incidence on their surface. If the incoming beam is not at normal incidence, the filter will have a lower transmission for the desired wavelength resulting in lower counts. Checking the back-reflection of the filters and re-coupling can fix this problem without disturbing the rest of the source. If there are a lot of problems with noise in the state that alignment isn't solving the filters may be letting too much of the pump through. Another less dominant source of noise is higher order effects from down-converting in a periodically poled material. As described in section 1.7, the Fourier series representation

of the nonlinear permittivity is:

$$\chi^{(2)}(z) \approx \sum_{n=-\infty}^{\infty} \frac{2\chi_0^{(2)}}{\pi n} \sin(\frac{\pi n}{2}) \exp(\frac{i2\pi nz}{\Lambda}). \tag{2.2}$$

We can pick out one term, or value of n to phase match and it will be dominant; however, the other terms can cause the creation of photons at other wavelengths, creating noise in the state. Both this and the pump leakage can by checked by looking at the output through a spectrometer with single-photon sensitivity. Getting a higher-quality low-pass filter, or multiple filters will solve the pump problem, and putting in a band-pass filter at the appropriate wavelength will get rid of higher order effects from the down-conversion.

2.5.3 Wave Plates

All three of the wave plates should be calibrated with respect to the PBS in the Sagnac triangle. This can be checked with minimal disturbance to the rest of the source. The first HWP (this sets the polarization of the pump) can be calibrated by blocking the horiztonal port of the PBS and placing a power meter in the vertical exit port. Rotate the wave plate to minimize the power and this will give the zero for the wave plate and the horizonal pump setting. For the second HWP (inside the Sagnac triangle) set the pump horizontal and place the power meter in front of the QWP by coupler "A" . Turn the HWP to minimize the power, this is a setting of 45° for the HWP. Also check to make sure the beam is going through the centre of the wave plates, and the HWPs should be back-reflected.

2.5.4 Crystal

There are two main things to consider when trying to fix the crystal alignment: linear translation and tilt. Try the linear translation first. If the crystal is back-reflected properly there should be minimal coupling changes so the singles shouldn't decrease much with translation. This is a good check to see if the crystal is indeed tilted properly. If the singles remain high, and low coincidences are the issue it could be the crystal isn't quite equidistant along the two paths and should be translated along the beam until maximum coincidences are found.

2.5.5 Dichroic Mirror

First check to see that the beam is indeed going through the centre of the dichroic mirror. Next it should have been aligned to reflect the beam coming out of the Sagnac triangle by 90°. Assuming the beam was originally lined up along the holes in the optical table (which it should have been) the reflected beam should also line up along the holes. Placing two irises in, one close to the dichroic and one as far away as possible, will reveal if this is indeed the case.

2.5.6 Lens

First check to make sure the beam is in the exact centre of the lens and that the lens is back-reflected. Ideally the lens should be on a translation stage along the line of the incoming beam, which will allow for fine tuning the distance from the crystal. If the beam is not focused properly on the centre of the crystal, this can seriously hurt the efficiency of the down-conversion process. It is important to do the appropriate calculations first to ensure the lens choice and approximate distance from the crystal are correct. The lens translation will have to be fine tuned from this point to maximize coincidences, and can always be put back in the approximate same place (if it gets bumped or needs to be replaced) and fine tuned to maximize coincidences.

2.5.7 Polarizing Beam Splitter

The beam splitter is one of the most difficult elements to trouble-shoot as it is very difficult to realign if moved. It is recommended to start with some visible cues before doing anything drastic. If you are working with a cube beam splitter, and the clamp that is holding it to the mount is pressing on the diagonal joint holding the two faces together, then the beam splitter will not behave optimally and will hurt the quality of the state. Space is often very tight in a Sagnac, so be sure to check that none of the beams exiting or entering the beam splitter are being clipped, and that they are all well-centred on the beam splitter face. If there are concerns about the quality of the beam splitter you can easily characterize it with

a polarizer in the incoming beam, and check the output power in the two output ports. If the beam splitter leaks too much horizontal light into the vertical port, or too much vertical light into the horizontal port, this will hurt the visibility of the output state. If the beam splitter angle or placement needs to be adjusted it is best to use irises and not touch any other elements until you have confirmed it has been correctly placed (See the appendix for more detailed instructions on how to replace this element).

Chapter 3

An Experimental Test of Three Families of Bell's Inequalities

3.1   Notes and Acknowledgements

In this chapter we successfully test three new families of Bell inequalities using the entangled photon Sagnac source, showing close agreement to the theoretical predictions of Wolfe and Yelin [12].

Notice: The contents of this chapter have been published in: L. Vermeyden, M. Bonsma, C. Noel, J. M. Donohue, E. Wolfe. and K. J. Resch, Phys Rev. A **87**, 2105 (2013).

Author Contributions KJR conceived the idea for the experiment LV and MB performed the experiment and analyzed the data. CN contributed to the initial assembly of the experiment. JD wrote the necessary Labview code. LV and MB jointly produced the first draft. All authors contributed to editing the final version.

3.2 Introduction

Quantum mechanics is one of the most well-tested and precise predictive theories in physics. Many of the features predicted by the quantum mechanical formalism are strange, yet the rapidly growing field of quantum information science is finding application for them in powerful new technologies [8]. One of the strangest and most important features of quantum mechanics was discovered by John Bell in that quantum predictions cannot be explained by local realistic descriptions of nature [36]. This discovery was expressed in the form of mathematical inequalities that were refined by subsequent work [11]. Bell's inequalities can place bounds on correlations imposed by local and nonlocal realistic theories [37, 38] and can be used as witnesses to detect entanglement [39]. They are applied in emerging technologies such as quantum key distribution [40, 41], quantum communication complexity results [42], certification of random number generation [43], and lowering error rate in classical communication schemes [44].

Bell's inequalities have been the subject of a wide variety of experiments, from early experiments using polarization-entangled photon sources from atomic cascades [45, 46] to later experiments using bright sources from parametric down-conversion [47, 48, 49, 50, 51] and other physical systems [52, 53]. The inequalities have also been extended theoretically to include larger numbers of particles [38, 54, 55, 56, 57, 58, 59, 60, 61], more measurement settings [62] and higher dimensional quantum systems [63]. Three families of Bell inequalities were recently investigated in Ref. [12] which have important consequences for comparing quantum correlations to those governed by local hidden variable models. The most well-known examples of Bell inequalities and tests of nonlocality [36, 11, 38, 54, 55] achieve maximal violation using maximally entangled states, such as Bell states or GHZ states [54], which have unpolarized subsystems and hence zero marginal expectation values. In contrast, two of new families of inequalities include contributions from marginal expectation values which in general require non-maximally entangled states to achieve maximal violations; they are furthermore able to explore a larger volume of correlation, as quantified by the analysis in Ref. [35], providing new insights into the limits quantum correlations. In the present work, we subject these new families of Bell inequalities to experimental test

Family	c_1	c_2	c_3	c_4	c_5	c_6	c_7	c_8	LHVM_{Max}	QM_{Max}
QB1	0	0	0	0	1	1	1	x	$\|x+1\|+2$	$x+3 \quad \forall x \geq -\frac{1}{3}$ $\sqrt{\frac{(x-1)^3}{x}} \quad \forall x < -\frac{1}{3}$
QB2	x	0	0	0	1	1	1	-1	$\|x\|+2$	$\|x\|+2 \quad \forall \|x\| \geq 2$ $\sqrt{2x^2+8} \quad \forall \|x\| < 2$
QB3	x	x	$-x$	0	1	1	1	-1	$3\|x\|-2 \quad \forall x \geq 2$ $\|x\|+2 \quad \forall \|x\| < 2$	$3\|x\|-2 \quad \forall x \geq 2$ $\|x\|+2 \quad \forall 1 \leq \|x\| < 2$ $\frac{\sqrt{(2-x^2)(4-3x^2)}-x^2}{1-x^2} \quad \forall x < 1$

Table 3.1: Three new families of Bell inequalities: QB1, QB2, and QB3. The coefficients defining the Bell operators are shown. Also shown are the maximum bounds for the Bell parameter, $\langle Z \rangle$, using the local hidden variable model (LHVM) and the quantum mechanical model (QM) [12].

over a wide range of parameters using entangled photons.

Consider a bipartite system with measurement settings A_i and B_j for particles 1 and 2, respectively, with outcomes $a_i = \pm 1$ and $b_j = \pm 1$, respectively. Expectation values of joint, or two-particle, measurements can be expressed as $\langle A_i B_j \rangle = P(a_i = b_j) - P(a_i = -b_j)$, i.e., the difference between the probability that the two outcomes are the same and the probability that they are different. Expectation values of marginal measurements can be expressed as $\langle A_i \rangle = P(a_i = 1) - P(a_i = -1)$, which is the difference between the probability of measuring $+1$ and the probability of measuring -1. Ref. [12] introduced a two-particle Bell operator Z,

$$
\begin{aligned}
Z \;\equiv\;& c_1 A_0 + c_2 A_1 + c_3 B_0 + c_4 B_1 + c_5 A_0 B_0 \\
&+ c_6 A_1 B_0 + c_7 A_0 B_1 + c_8 A_1 B_1,
\end{aligned}
\tag{3.1}
$$

where the c_i are real constants. Note that Z contains both two-particle and single-particle operators. Three families of Bell's inequalities, QB1, QB2, and QB3, were derived from the operator Z using parameterized sets of the coefficients, c_i, as shown in Table 3.1. In each family, the c_i are either constant or depend on a single adjustable parameter x. Local hidden-variable models (LHVM) result in upper limits for the Bell parameter, $\langle Z \rangle$, which were shown to be functions of x. These Bell's inequalities are violated by quantum mechanics (QM) over specific ranges of x in each family. The bounds derived in Ref. [12] for LHVM and QM are shown in Table 3.1. The CHSH inequality [11] is perhaps the most well-known Bell inequality. Each new family of Bell inequalities considered here includes the CHSH inequality as a special case; specifically QB1, QB2, and QB3 reduce to the CHSH inequality for parameter values $x = 1$, $x = 0$, and $x = 0$, respectively. Maximal violation of the CHSH inequality can be achieved with a two-qubit maximally entangled state, such as a Bell state. However, maximally entangled states have completely unpolarized subsystems, and thus any single-particle, or marginal, expectation value $\langle A_i \rangle, \langle B_j \rangle$ for a maximally entangled state is 0.

The inequalities QB2 and QB3 contain single-particle expectation values. For these marginals to have an impact on the Bell parameter $\langle Z \rangle$, the particles must have partially-
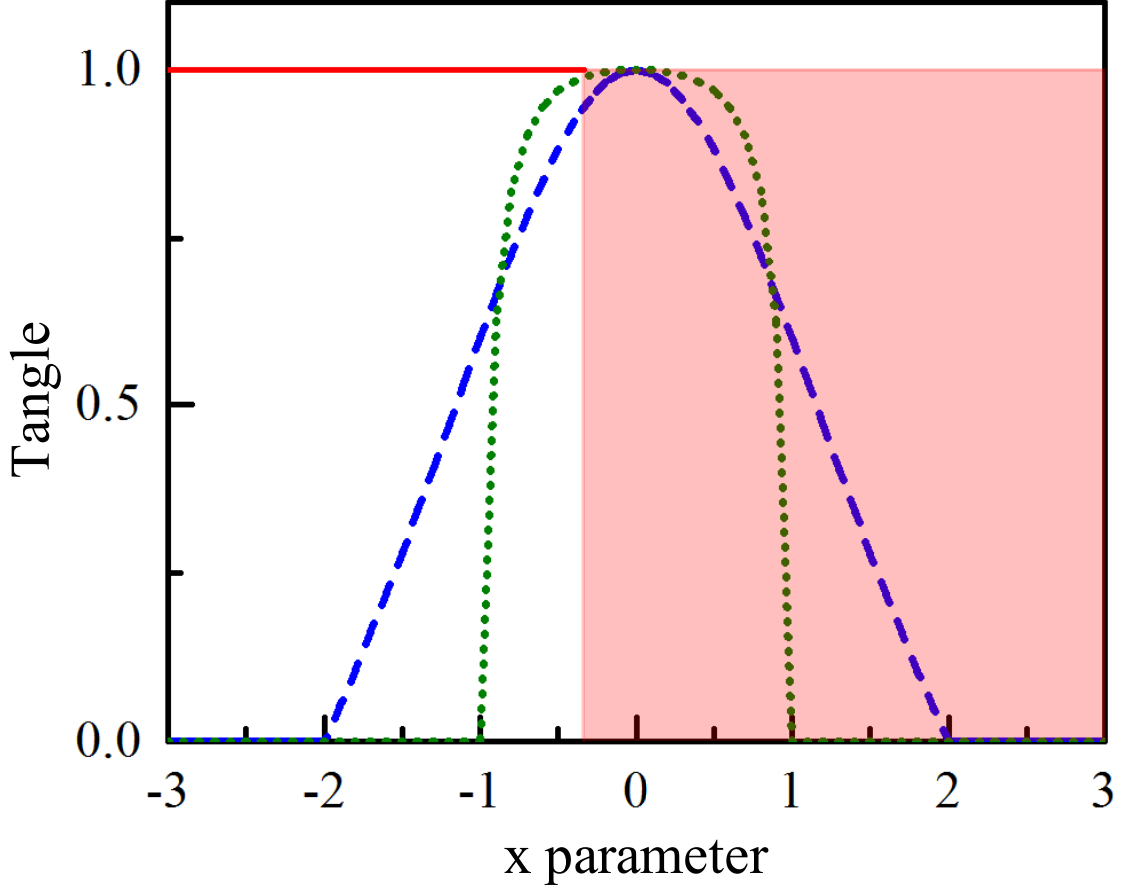
Figure 3.1: Optimal tangle [10] required to achieve the maximum Bell parameter. These plots show the numerically calculated tangle, τ, of a state of the form of Eq. 3.2 which achieves the maximum Bell parameter as a function of x for QB1 (solid red), QB2 (dashed blue), and QB3 (dotted green). (A state with $\tau = 1$ is maximally entangled while $\tau = 0$ indicates no entanglement; non-maximally entangled states have a value $0 < \tau < 1$.) QB2 and QB3 in general require non-maximally entangled states to achieve the largest Bell parameter. For QB1 the optimal tangle is $\tau = 1$ until $x < -1/3$. For $x \geq -1/3$ the maximum value of $\langle Z \rangle$ can be reached with any amount of entanglement, which we represent by a shaded region, but there can be no Bell inequality violation since QM and LHVM models predict the same bound. The tangle can be expressed in terms of the angle α in Eq. 3.2 by the relation $\tau = \sin^2 (2\alpha)$. [40].

polarized subsystems which arise in *non-maximally*-entangled states. It is also unclear *a priori* if the unequal magnitude coefficients of the joint expectation values in QB1 would require non-maximally entangled states to optimize the Bell inequality violations. To investigate this, we consider entangled states of the form

$$|\psi(\alpha)\rangle = \cos\alpha|HH\rangle + \sin\alpha|VV\rangle, \qquad (3.2)$$

where the angle α is an adjustable parameter that determines the amount of entanglement. We represent each measurement setting, A_i and B_j, with an operator $\vec{\sigma}\cdot\hat{n}$, where $\vec{\sigma} = (\sigma_x, \sigma_y, \sigma_z)$ is a vector of Pauli matrices and the unit vector $\hat{n} = (\sin\theta\cos\phi, \sin\theta\sin\phi, \cos\theta)$ where choice of the angles determines the setting. Using the MATHEMATICA function NMAXIMIZE, we find the state and measurement settings which maximize the Bell parameter $\langle Z \rangle$ for each Bell inequality for each value of the parameter x.

In Fig. 4.2 we plot the amount of entanglement, as characterized by the tangle ($\tau = \sin^2(2\alpha)$ given our parametrization of the state) [10], required to maximize $\langle Z \rangle$ as a function of the parameter, x, for QB1 (solid red line), QB2 (dashed blue line), and QB3 (dotted green line). For the Bell inequality QB1, a maximally entangled state is needed to reach the maximum violation when $x < -1/3$; for $x \geq 1/3$ there exist states with any amount of entanglement which can achieve the maximum expectation value of Z, which we depict as the red region, but no violation of Bell's inequality is possible in this regime since the LHVM and QM maxima coincide. For QB2 and QB3, Bell inequality violations are possible when $|x| < 2$ and $|x| < 1$, respectively. In these regions non-maximally entangled states are required to achieve the maximum Bell inequality violation. The only exceptions are the cases where $x = 0$, reducing these inequalities to the CHSH inequality which requires a maximally entangled state for maximum violation. To effectively test these new inequalities over the largest possible parameter space requires a source of entangled photons with variable entanglement.
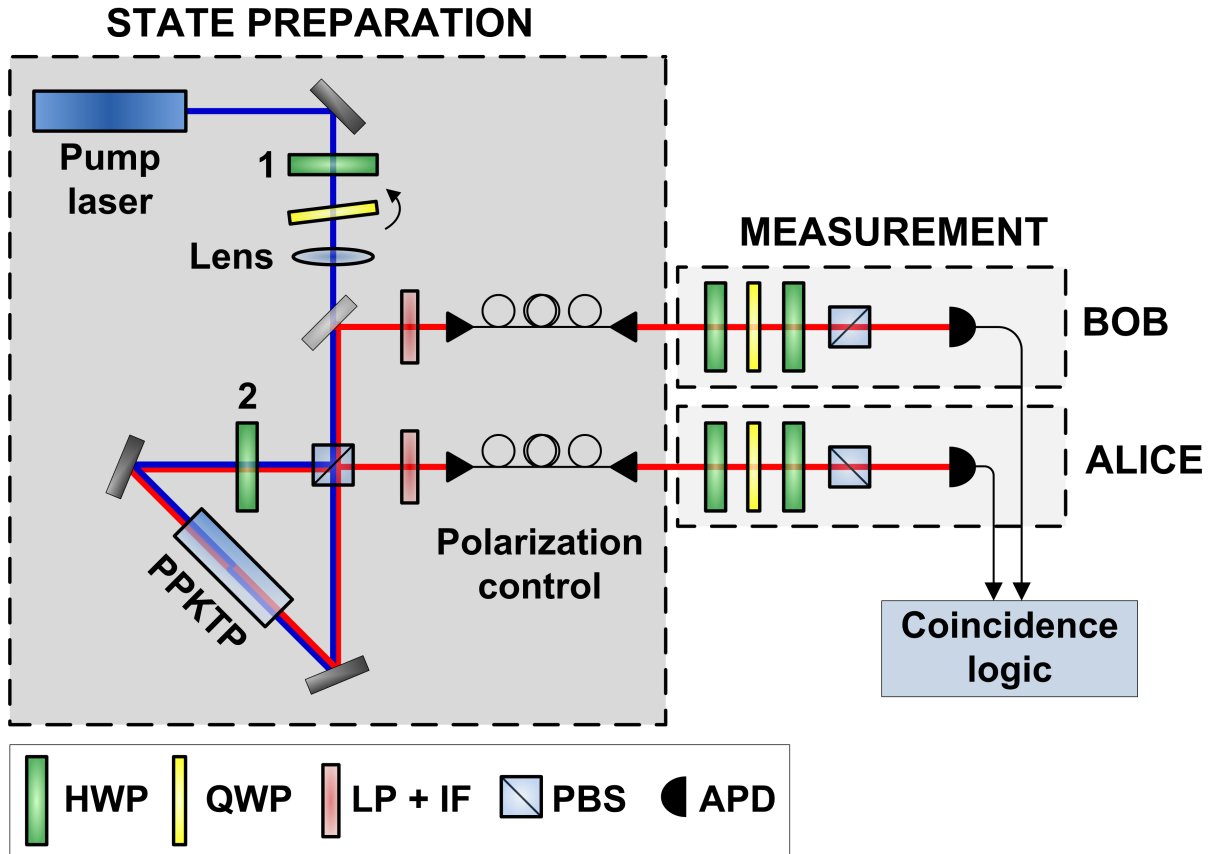
Figure 3.2: Experimental setup. Pairs of polarization-entangled photons were generated via spontaneous-parametric down-conversion and measured using two polarization analyzers. The pump beam was rotated using a half-wave plate (HWP) and quarter-wave plate (QWP), then focused on a periodically-poled KTP (PPKTP) crystal. The down-converted photons traveled though long-pass (LP) and band-pass interference (IF) filters to remove any remaining pump signal before coupling into single-mode fibres. Projective measurements were taken, and photons were detected with silicon avalanche photo-diodes (APDs) and analyzed with coincidence logic.

3.3 Experiment

Our experimental setup is shown in Fig. 4.1. In the state-preparation part of the experiment, polarization-entangled photon pairs are generated using parametric down-conversion in a polarization-based Sagnac interferometer [64, 65, 66]. A $5\,mW$ CW diode pump laser with centre wavelength $404.8\,nm$ is focused on a $20\,mm$ PPKTP crystal, phase-matched to produce photon pairs at $809.8\,nm$ and $809.3\,nm$ from type-II nearly degenerate down-conversion. The polarizing beamsplitter (PBS) in the source splits the pump beam into two components, one circulating in a clockwise direction and the other in a counter-clockwise direction. HWP2 inside the interferometer ensures that the pump beam enters the crystal with horizontal polarization in both directions. The photon pairs are thus created in a superposition of propagation direction (clockwise or counter-clockwise) in the interferometer and are converted into polarization entanglement upon recombination at the PBS. After emerging from the PBS, the light is coupled into single-mode fibres containing polarization controllers to direct the light to the polarization analyzers. The polarization of the pump laser is controlled using HWP1 and a quarter-wave plate (QWP) oriented at $0°$ and tilted. In conjunction with the polarization controllers, these waveplates enable production of the non-maximally entangled states of the form shown in Eq. 3.2.

The photon pairs emerge from fibres in the measurement part of the experiment. We used the angles of first two wave plates, a HWP followed by a QWP, to determine the basis for the measurement. The final HWP was set to either $0°$ or $45°$ to measure the $+1$ and -1 outcomes, respectively, for a given measurement setting. After the analyzer wave plates, the photons in the transmitted ports of the PBSs were coupled into single-mode fibres and directed to single-photon counting detectors (Perkin-Elmer SPCM-AQ4C), labelled Alice and Bob, from which coincidence events were recorded with an 3 ns window. Typical rates were about 25 kCps for singles counts and 1.4 kCps for coincidence counts.

We begin by characterizing the states produced by our source. We use $|H\rangle$ and $|V\rangle$ to describe the horizontal and vertical polarization states; we use the notation $|D\rangle = \frac{1}{\sqrt{2}}(|H\rangle + |V\rangle)$, $|A\rangle = \frac{1}{\sqrt{2}}(|H\rangle - |V\rangle)$, $|R\rangle = \frac{1}{\sqrt{2}}(|H\rangle - i|V\rangle)$, and $|L\rangle = \frac{1}{\sqrt{2}}(|H\rangle + i|V\rangle)$. We performed quantum state tomography on the coincidence counts from an overcomplete

44
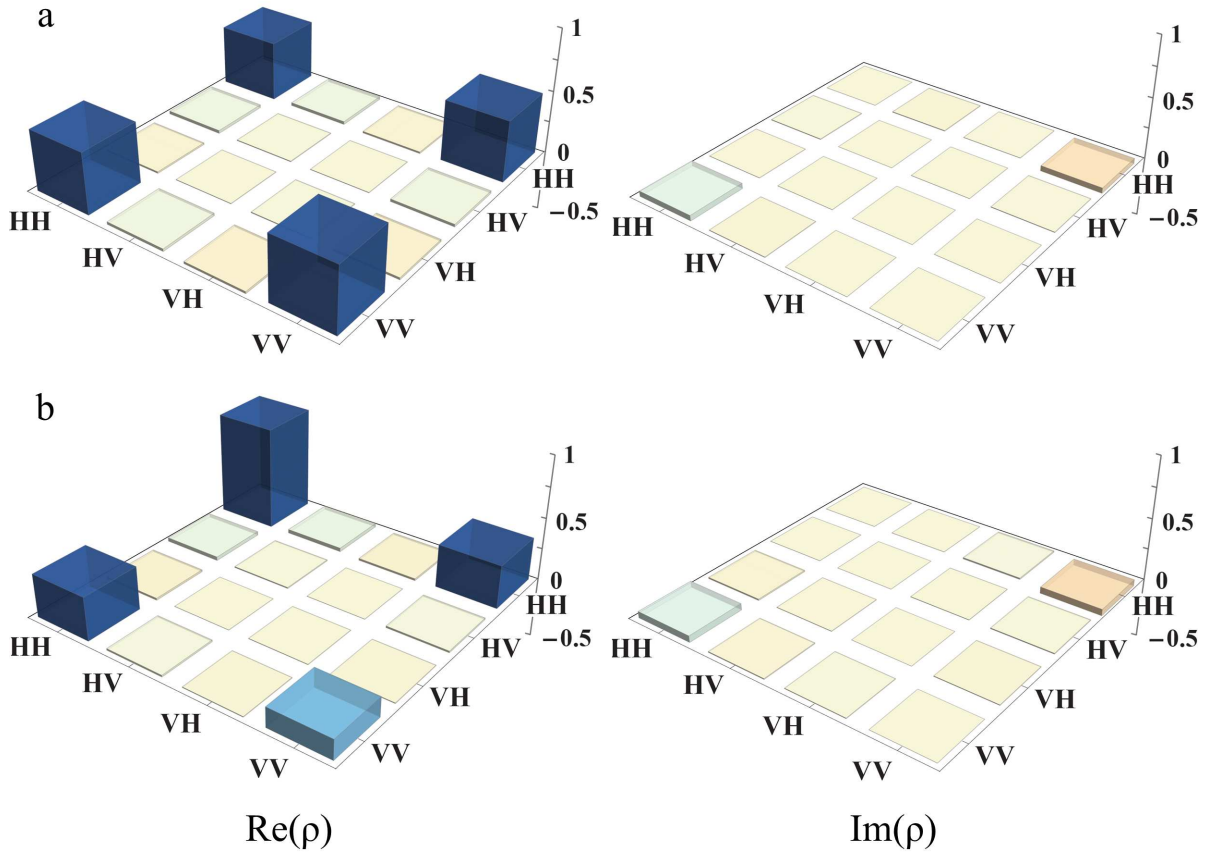
Figure 3.3:   Reconstructed density matrices.   Quantum state tomography was performed on two sample states, a) where the target was the maximally entangled state $|\psi(45°)\rangle = \frac{1}{\sqrt{2}}(|HH\rangle + |VV\rangle)$ and b) where the target was the non-maximally entangled state $|\psi(22°)\rangle = \cos 22°|HH\rangle + \sin 22°|VV\rangle$. The density matrices were reconstructed from our experimental data using the maximum likelihood method in Ref. [16]. Fidelities with the target states were a) 0.982 and b) 0.978.

set of polarization measurements $|H\rangle$, $|V\rangle$, $|D\rangle$, $|A\rangle$, $|R\rangle$, and $|L\rangle$ for each photon and a measurement time of $3\,s$ per setting. The experimental density matrix was reconstructed using the maximum likelihood iterative method from Ref. [16]. Sample reconstructed density matrices are shown in Figs. 4.3a) and b) for the maximally entangled target states $|\psi(45°)\rangle$ and the non-maximally entangled state $|\psi(22°)\rangle$. The fidelity [67] of these states with their target states are 0.982 and 0.978 for a) and b) respectively. These fidelities were representative of those states measured for other values of α.

To experimentally test the Bell inequalities, we chose the state and measurement settings at the analyzer to obtain the maximum theoretical value of the Bell parameter as predicted by our numerical optimization. To extract each joint expectation value, we configured the measurement settings using the first HWP and QWP in each analyzer, then measured 4 coincidence counts corresponding to the four combinations of ± 1 outcomes on each side using the final HWPs. The inequalities QB2 and QB3 require marginal expectation values and these were extracted from coincidence measurements by averaging results from those cases where the relevant operator appeared in a joint expecation value. For example, our measurement of the marginal $\langle A_0 \rangle$ was extracted from the coincidence counts taken when measuring $\langle A_0 B_0 \rangle$ and $\langle A_0 B_1 \rangle$. We collected Bell measurements with a measurement time of $1\,s$ for each waveplate setting.

3.4 Results and Discussion

Our experimental results can be found in Fig. 3.4. The measured Bell parameter is plotted as a function of the parameter, x, for a) QB1, b) QB2, and c) QB3. The maximum theoretical values (see Table 3.1) possible according to quantum mechanics are shown as a solid line while the maximum value from a local hidden variable model are shown as a dotted line. Any experimental data points with a value greater than the LHVM dotted line violate the corresponding Bell inequality. It is clear from these plots that our data indeed violate these families of inequalities over a large range of parameters.

To explore the range of parameters where we observe a violation, we plotted the value
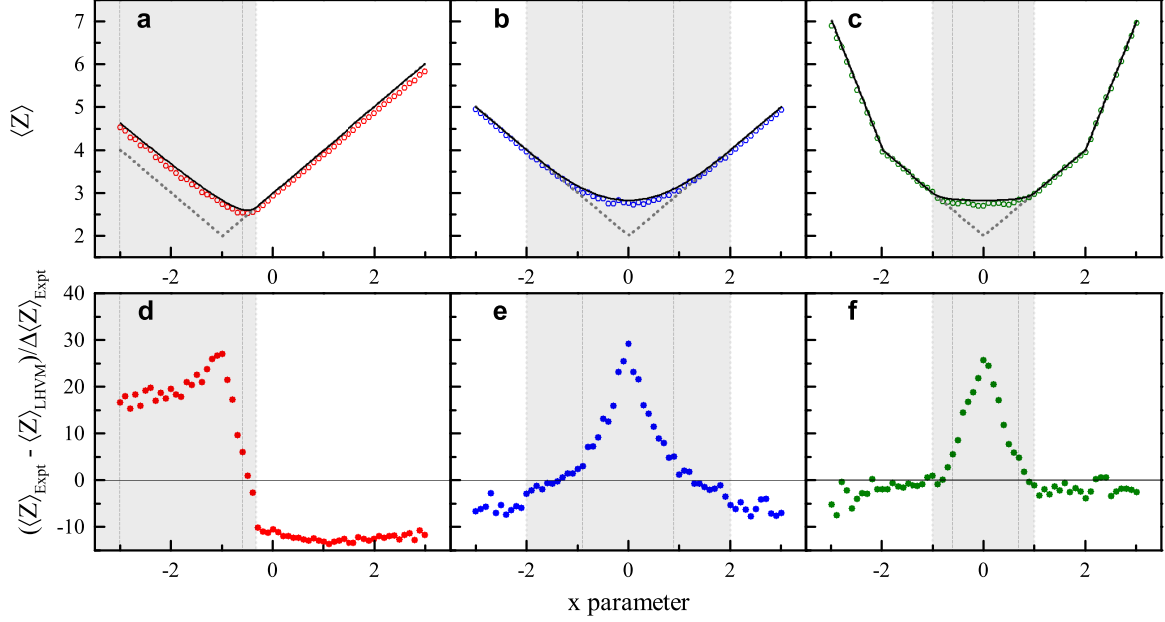
46

Figure 3.4: Experimentally measured Bell parameters for three families of Bell inequalities. The measured values for the Bell inequalities a) QB1, b) QB2, and c) QB3 are shown as a function of the parameter x. The experimentally measured values are shown as circles, and the solid line shows the theoretical quantum limit. The theoretical bounds imposed by local hidden variable models (LHVM) are shown as a dotted line. Error bars were not included for parts a)–c) because they were smaller than the size of the data points. In panels d)–e), we plot a function N, which, when positive, is the number of standard deviations of violation of the Bell inequality versus x. The shaded areas in panels a)–e) indicate regions where a Bell inequality violation is possible, and the vertical lines inside this region show the range over which our experiment achieved a 3σ or greater violation. For QB1, we found a 3σ or greater violation between $x = -3$ (largest negative value tested) and $x = -0.6$. For QB2, we found a 3σ or greater Bell violation between $x = -0.9$ and $x = 0.9$, which represents 49% of the total possible range according to quantum mechanics. For QB3, the range of 3σ violation or greater was between $x = -0.6$ and $x = 0.7$, representing 74% of the range possible according to quantum theory.

47

of the function $N = \left(\langle Z \rangle_{Expt} - \langle Z \rangle_{LHVM}\right)/\Delta\langle Z \rangle$ versus x, where $\langle Z \rangle_{Expt}$ is the experimentally measured Bell parameter, $\Delta\langle Z \rangle$ is the standard deviation in that result, and $\langle Z \rangle_{LHVM}$ is the maximum value allowed by LHVM. If the value of the function N is positive, then it quantifies the size of the violation in terms of number of standard deviations over the maximum local hidden variable prediction. If N is negative, then no violation was observed. The results of these measurements are shown in Fig. 3.4d)–f). The maximum violation, in terms of number of σ, occurred for QB2 and QB3 at $x = 0$, and for QB1 at $x = -1$. In these three particular cases each inequality reduces to the familiar CHSH inequality. Theoretically it is possible to observe a violation over a specific range of parameters; these ranges are depicted as the shaded grey regions in each plot. However, comparing these regions to the theoretical lines in Fig. 3.4a)–c), we see that near the borders the maximum QM and LHVM values converge making Bell violation experimentally very challenging. Using Poissonian errors for the experimentally measured counts, we calculated N as a function of x in Figs. 3.4d)–f). We estimated the range of x over which significant, $> 3\sigma$, violation of the inequalities was achieved. We found $x \leq 0.6, |x| \leq 0.9$, and $-0.6 \leq x \leq 0.7$ for QB1, QB2, and QB3 respectively. For QB2 and QB3 this corresponds to a range which is 49% and 74%, respectively, of the theoretically possible range. (We do not include such a measure for QB1 since the range of x over which theory predicts a violation is semi-infinite.)

3.5   Conclusion

We have experimentally tested the three families of Bell inequalities derived in Ref. [12]. We identified the specific relationship between maximal violation of each Bell inequality and the entanglement of the associated quantum state. We have measured very good agreement with theory and shown strong violations of the inequalities, up to 29σ, over a wide range of the parameters. We have demonstrated significant violation of the inequalities QB2, and QB3 over 49% and 74% respectively of the theoretically possible range of parameters. Our results serve as a benchmark for these Bell inequalities, as extending the range violations significantly will require substantive improvements in source fidelity and photon pair production rates.

Chapter 4

An Experimental Test of Envariance

4.1 Notes and Acknowledgements

This chapter is being incorporated into a paper for publication with the following authors: L. Vermeyden, J. Lavoie, M. Bonsma, X. Ma, U. Sinha, R. Laflamme and K. J. Resch.

Author Contributions RL and KJR conceived the idea for the experiment. KJR, JL and LV designed the experimental setup. LV performed the experiments, analyzed the data and wrote the first paper draft. MB and JL contributed to building the experimental setup. XM, US, and RL provided theoretical support. All authors contributed to writing the final manuscript.

4.2 Introduction

Symmetries play a central role in physics with wide-reaching implications in fields as diverse as spectroscopy and particle physics. It is therefore of fundamental importance to identify and understand new symmetries of nature. One recently identified symmetry in quantum mechanics has been named environment-assisted invariance, or *envariance* [14]. It applies

in certain cases where a composite quantum object consists of a system part, labelled S, and an environment part, labelled E. If some action is applied to the system part only, described by some unitary transformation, U_S, then the state is said to be envariant under U_S if another unitary applied to the environment, U_E, can restore the initial state. For pure quantum states, this can be expressed,

$$U_S|\psi_{SE}\rangle = (u_S \otimes \mathbb{1}_E)|\psi_{SE}\rangle = |\eta_{SE}\rangle \tag{4.1}$$

$$U_E|\eta_{SE}\rangle = (\mathbb{1}_S \otimes u_E)|\eta_{SE}\rangle = |\psi_{SE}\rangle. \tag{4.2}$$

Envariance is an example of an assisted symmetry [15] where once the system is transformed under some unitary U_S, it can be restored to its original state by another operation on a physically distinct system: the environment.

Envariance is a uniquely quantum symmetry in the following sense. A pure quantum state represents complete knowledge of the quantum system. In an entangled quantum state, however, complete knowledge of the whole system does not imply complete knowledge of its parts. It is therefore possible that an operation on one part of a quantum state can alter the global state, but its local effects are masked by incomplete knowledge of that part; the effect on the global state can then be undone by an action on a different part. In contrast, complete knowledge of a composite classical system implies complete knowledge of each of its parts. Thus transforming one part of a classical system cannot be masked by incomplete knowledge and cannot be undone by a change on another part.

Envariance plays a prominent role in work related to fundamental issues of decoherence and quantum measurement [14, 69, 15]. Decoherence converts amplitudes in coherent superposition states to probabilities in mixtures and is central to the emergence of the classical world from quantum mechanics [70, 71]. Mathematically the mixture appears in the reduced density operator of the system which is extracted from the global wavefunction by a partial trace [72, 8]. This partial trace limits the approach for deriving, as opposed to separately postulating, the connection between the wavefunction and measurement probabilities known as Born's rule [1], since the partial trace *assumes* Born's rule is valid [14, 73]. Envariance was employed in a derivation of Born's rule which sought to avoid circularity inherent to approaches which rely on partial trace [14]. For comments on this derivation, see for example [73, 75, 74].

4.3   Experiment

In the present work, we subject envariance to experimental test in an optical system. We use the polarization of a single photon to encode the system, S, and the polarization of a second single-photon to encode the environment, E. A single-photon is not as complex as most natural environments; however we require precision control over the environment component, necessitating a relatively simple quantum system. We subject the system photon to a wide range of polarization rotations with the goal of bench-marking the degree to which we can restore the initial state by applying a second transformation on the environment photon.

Our test requires a source of high-quality two-photon polarization entanglement, an optical set-up to perform unitary operations on zero, one, or both of the photons, and polarization analyzers to characterize the final state of the light. Our experimental setup is shown in Fig. 4.1. We produce pairs of polarization-entangled photons using spontaneous parametric down-conversion (SPDC) in a Sagnac interferometer [64, 65, 66]. In the ideal case, this source produces pairs of photons in the singlet state,

$$|\psi_{\mathsf{SE}}\rangle = \frac{1}{\sqrt{2}} \left(|H\rangle_{\mathsf{S}} |V\rangle_{\mathsf{E}} - |V\rangle_{\mathsf{S}} |H\rangle_{\mathsf{E}} \right), \tag{4.3}$$

where $|H\rangle$ ($|V\rangle$) represents horizontal (vertical) polarization, and S and E label the photons. This state is envariant under all unitary transformations and has the convenient symmetry that $U_{\mathsf{S}} = U_{\mathsf{E}}$ for all U_{S}. We pump a 20 mm periodically-poled KTP crystal (PPKTP), phase-matched to produce photon pairs at 809.8 nm and 809.3 nm from type-II down-conversion using 6 mW from a CW diode pump laser with centre wavelength 404.8 nm. The output from the source is coupled into single-mode fibres, where polarization controllers correct unwanted polarization rotations in the fibre. The light is coupled out of the fibres and directed to two independent polarization analyzers. Each analyzer consists of a half-wave plate (HWP), quarter-wave plate (QWP), and a polarizing beam-splitter (PBS). Between the fibre and the analyzers are two sets of wave plates—a QWP, a HWP, then another QWP—which can be inserted as a group into the beam paths to implement controlled polarization transformations. Photons from both ports of each PBS are detected using single-photon counting modules (Perkin-Elmer SPCM-AQ4C) and
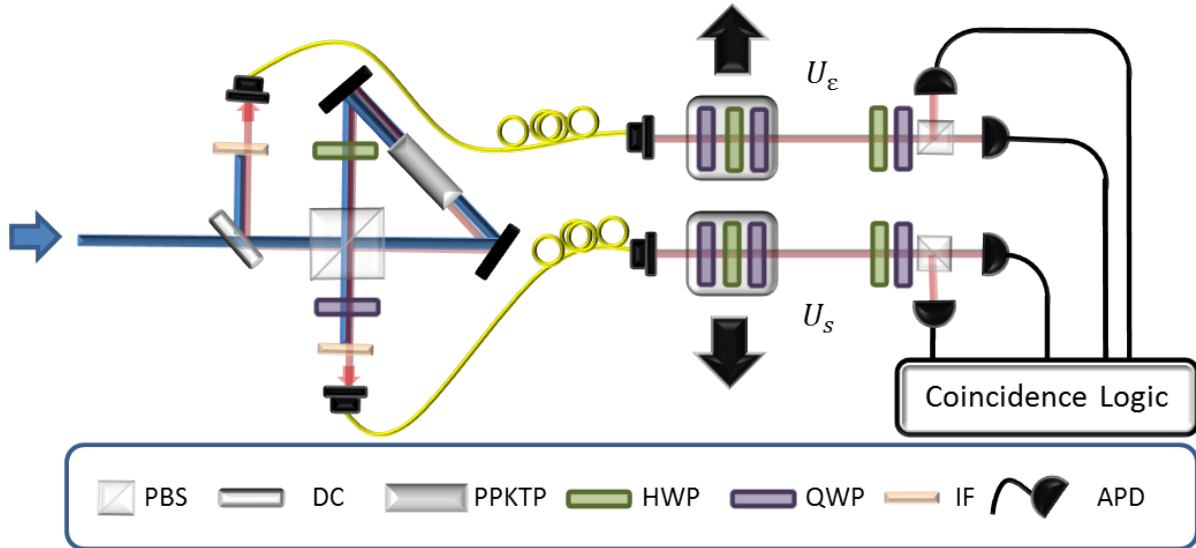
Figure 4.1: Experimental setup. The entangled photon pairs are created using type-II spontaneous parametric down-conversion. The pump laser is focused on a periodically-poled KTP crystal and pairs of entangled photons with anti-correlated polarizations are emitted. The pump is filtered using a band-pass filter, and polarization controls adjust for the alterations due to the coupling fibres. The entangled photon pairs are set so one photon is considered the system, and the other is considered the environment. After the source the unitary transformations are applied. A three wave plate combination is required to apply an arbitrary unitary transformation: quarter wave-plate (QWP), half wave-plate (HWP), QWP. A set of this combination of wave plates is mounted on each translation stage which can slide the wave plates in and out of the path of the incoming photons. The photons are then detected using polarizing beam splitters (PBS) and two wave plates to take projective measurements. The counts are then analyzed using coincidence logic.

Rotation Axis	$\alpha(\theta)$	$\beta(\theta)$	$\gamma(\theta)$
$\hat{x}$	$\pi/2$	$-\theta/4$	$\pi/2$
$\hat{y}$	$\pi/2 + \theta/2$	$\theta/4$	$\pi/2$
$\hat{z}$	$\pi/4$	$-\pi/4 - \theta/4$	$\pi/4$

Table 4.1: Wave plate settings used to implement polarization rotations. The angles α, β and γ are the wave plate angles for the first QWP, the HWP and the second QWP respectively. The angle θ is the rotation angle of the polarization about the specified axis on the Bloch sphere.
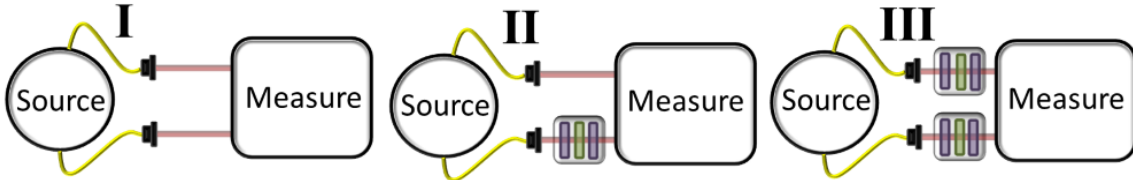

Figure 4.2: Experimental measurement procedure. We investigated the impact of each unitary transformation by performing quantum state tomography at three different stages: directly on the initial state with no unitary transformations (**I**), on the state with a transformation applied to the system photon (**II**), and on a state with the same transformation applied to both the system and environment photon (**III**).

analyzed using coincidence logic with a 1 ns coincidence window, counting for 5 s. We typically measured total coincidence rates of 5.4 kHz across the four detection possibilities for photons S and E.

For our experiment, we implemented rotations about the standard $\hat{x}$, $\hat{y}$, and $\hat{z}$ axes of the Bloch sphere; in addition we implemented rotations about an axis $\hat{m} = (\hat{x} + \hat{y} + \hat{z})/\sqrt{3}$. The wave plate angles used to implement rotations by an angle θ about the $\hat{x}$, $\hat{y}$, and $\hat{z}$ axes are shown in Table 4.1; the angles to implement rotations about $\hat{m}$ were determined numerically using MATHEMATICA.

Our experiment proceeds in three stages as depicted in Fig. 4.2: first characterizing the initial state (**I**), then characterizing the state after a transformation is applied to the system photon (**II**), and finally characterizing the state after that same transformation is applied to both system and environment (**III**). We record a tomographically-overcomplete set of measurements at each stage, performing the 36 combinations of the polarization measurements, $|H\rangle$, $|V\rangle$, $|D\rangle = \frac{1}{\sqrt{2}}(|H\rangle + |V\rangle)$, $|A\rangle = \frac{1}{\sqrt{2}}(|H\rangle - |V\rangle)$, $|R\rangle = \frac{1}{\sqrt{2}}(|H\rangle + i|V\rangle)$, and $|L\rangle = \frac{1}{\sqrt{2}}(|H\rangle - i|V\rangle)$ on each photon and counting for 5 s for each setting. The states were then reconstructed using the maximum likelihood method from Ref. [16].
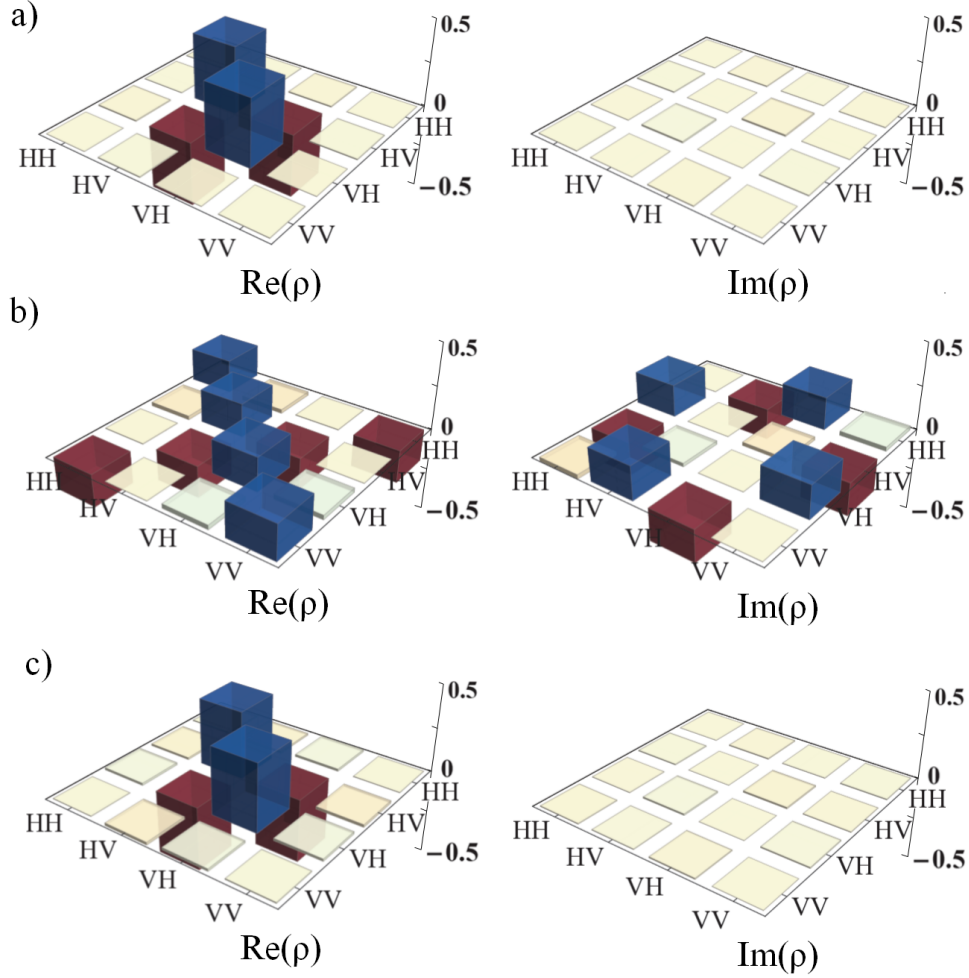
Figure 4.3: a) Is the real and imaginary parts of the reconstructed density matrix of the initial state from the source (stage **I** of the procedure). It has 0.987 fidelity [67] with the ideal. b) The system photon is transformed using wave plates set to implement the rotation of 90° about the $\hat{x}$ axis, stage **II**. The resulting density matrix shown has 0.488 fidelity with the ideal initial state, 0.501 with the initial reconstructed state and 0.995 with the expected state, calculated by transforming the density matrix from a). c) The reconstructed density matrix after the same unitary from b) is applied to both photons, stage III. This state has a 0.987 fidelity with the ideal, 0.995 with the reconstructed state from a), and 0.997 with the expected state calculated by transforming the state from part a).

This procedure was repeated for a diverse range of transformations. We configured our setup to implement unitary rotations in multiples of 30° from 0° to 360° about each of the $\hat{x}$, $\hat{y}$, $\hat{z}$, and $\hat{m}$ axes. The data acquisition time for this procedure over the set of 13 rotation angles about each axis was approximately six hours. The source was realigned before each run to achieve maximum fidelity with the singlet state from 0.985 to 0.990.

Figure 4.3a)–c) show the real and imaginary parts of the reconstructed density matrix of the quantum state at the three stages in the experiment, **I**, **II**, and **III** respectively. The fidelity [67] of the state during these samples of two of the stages are 0.987 for both **I** a), and **III** c), respectively, and is defined as [67]:

$$F(\rho, \sigma) = \{\text{Tr}[(\sqrt{\rho}\sigma\sqrt{\rho})^{1/2}]\}^2. \tag{4.4}$$

We can use this definition to calculate the fidelity between the state at stages **I** and **III**. Comparing between the states shown in Fig. 4.3 panels a) and c) the resulting fidelity is 0.995.
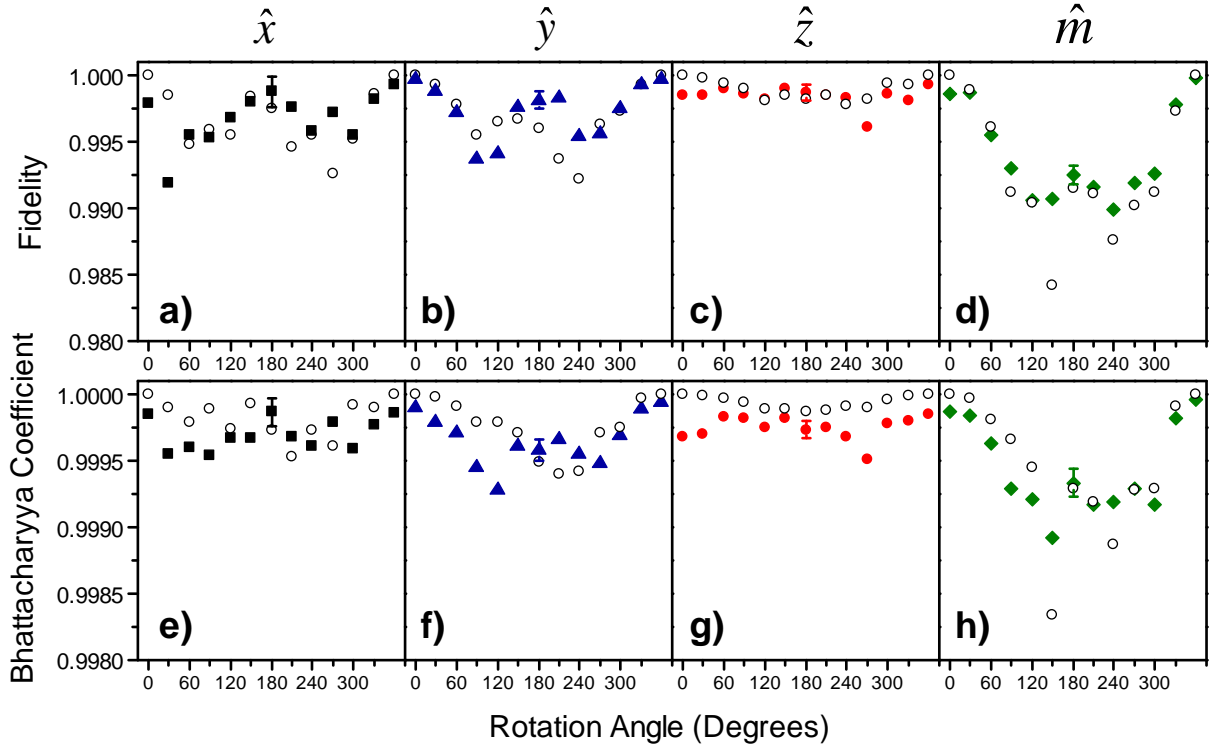
Figure 4.4: Analysis of the experimental results. Panels a)–d) show the fidelity analysis results for unitary rotations about $\hat{x}$, $\hat{y}$, $\hat{z}$, and $\hat{m}$ axes as functions of rotation angle. The coloured data points are the comparison between stage **I** and stage **III** (comparing the source state and the state after the unitary has been applied to both qubits). The open circles show a theoretical comparison. Panels e)–h) show the quantum Bhattacharyya results comparing stage **I** and stage **III** in the coloured data points for each of the four axis, with the open circles being the theoretical comparison. For plots which include a comparison of stage **I** and **II** (applying the unitary to one qubit only) and theoretical comparisons, see the appendix. The error bar for each graph is the standard deviation of comparisons of source state measurements during the experiment.

4.4   Results and Discussion

The summary of the results from our experiment is shown in Fig. 4.4. The coloured data points in Fig. 4.4a)–d) show the fidelity of the experimentally reconstructed state at stage **III** with the reconstructed state from the initial stage **I**, i.e., $F(\rho_{\mathrm{expt}}^{\mathbf{I}}, \rho_{\mathrm{expt}}^{\mathbf{III}})$, as a function of the rotation angle for rotations about the $\hat{x}$, $\hat{y}$, $\hat{z}$, and $\hat{m}$, respectively. The open circles show the theoretical expectation for the fidelity between the measured state at stage **I** with the expected state in stage **III**, calculated by acting the unitaries on the measured state from stage **I**, i.e., $F(\rho_{\mathrm{expt}}^{\mathbf{I}}, \rho_{\mathrm{th}}^{\mathbf{III}})$. The fidelities are very high, close to the limit of 1, in all cases and we see reasonable agreement with expectation.

We considered the effects of Poissonian noise and waveplate calibration on our results and found that these effects were too small to explain the deviation between $F(\rho_{\mathrm{expt}}^{\mathbf{I}}, \rho_{\mathrm{expt}}^{\mathbf{III}})$ and $F(\rho_{\mathrm{expt}}^{\mathbf{I}}, \rho_{\mathrm{th}}^{\mathbf{III}})$. To account for this, we characterized the fluctuations in the state produced by the source itself by comparing the state produced in subsequent stage **I** sates in the data collection; recall that stage **I** for each choice of unitary is always the same (no additional waveplates inserted) and thus provides a good measure of the source stability. Specifically, we calculated the standard deviation in the fidelity of the state produce at a stage I in the ith round of the experiment to that produced in the *next*, $(i + 1)^{\mathrm{th}}$, stage I, $F(\rho_{\mathrm{expt}}^{\mathbf{I},i}, \rho_{\mathrm{expt}}^{\mathbf{I},i+1})$. The standard deviation in these fidelities calculated from the data taken within each set of rotation axes are shown as representative error bars on the plots in Figs. 4.4a)–d). The standard deviation of this quantity over all the experiments was 0.0008. We characterize the difference between the measured and expected fidelities by calculating the standard deviation in the quantity, $F(\rho_{\mathrm{expt}}^{\mathbf{I}}, \rho_{\mathrm{expt}}^{\mathbf{III}}) - F(\rho_{\mathrm{expt}}^{\mathbf{I}}, \rho_{\mathrm{th}}^{\mathbf{III}})$, for each experiment. (This is the difference between the coloured and open data points in Figs. 4.4a)–d).) over all experiments to be 0.002. This value is comparable to the error in the fidelity due to source fluctuations. Refer to the appendix to see the comparison between stage **I** and stage **II**, which would not fit on the scale of Fig. 4.4.

From our data, we extract the average fidelity $F(\rho_{\mathrm{expt}}^{\mathbf{I}}, \rho_{\mathrm{expt}}^{\mathbf{III}})$ for the set of measurements made for each unitary axis and show the results in Table II. As measured by the average fidelity, our experiment benchmarks envariance to 0.9966 ± 0.0004,$((99.66 \pm 0.04)\%$ of the ideal) averaged over all rotations.

Rotation Axis	Average Fidelity	Average BC
$\hat{x}$	0.997 ± 0.001	0.9997 ± 0.0001
$\hat{y}$	0.9973 ± 0.0007	0.99966 ± 0.00008
$\hat{z}$	0.9984 ± 0.0006	0.99975 ± 0.00007
$\hat{m}$	0.9941 ± 0.0007	0.9994 ± 0.0001
Overall average:	0.9966 ± 0.0004	0.99963 ± 0.00005

Table 4.2: Summary of the results for comparing stages **I** and **III** using fidelity and Bhattacharyya Coefficient (BC) analysis and averaging over each unitary rotation. The overall average is representative of the overall envariance of our state.

Fidelity has conceptual problems as a measure for testing quantum mechanics, since tomography assumes quantum mechanics to reconstruct the density matrices required to compute the value. The Bhattacharyya Coefficient (BC) is a measure of the overlap of the probability distributions for discrete distributions where p_i and q_i are the probability of the ith element for each distribution, the BC is defined [3],

$$BC = \sum_i \sqrt{p_i q_i}. \tag{4.5}$$

If we normalize the measured tomographic data by dividing by the sum of the counts, we can treat this as a probability distribution. The BC then can be calculated using the distribution of measurements at each stage in the experiment, directly analogous to the approach used with fidelity. It should be noted that the BC has some limitations when applied in this case. If two quantum states produce identical measurement outcomes, its value is 1. Unlike fidelity though, it is not the case that the BC goes to 0 for orthogonal quantum states. For example, the BC for two orthogonal Bell states measured with an overcomplete set of polarization measurements is 7/9. Furthermore, the value of the BC is dependent on the particular choice of measurements taken. While we are employing a commonly-used measurement set for characterizing two qubits, other choices would produce different BCs. Nevertheless, this metric can be employed to quantify the envariance in our experiment without quantum assumptions, making it appropriate for testing quan-

tum mechanics.

Our experiment procedure included three stages, **I** measurements of the source, **II** measurements after we apply the unitary to only one qubit, and **III** measurements after applying the same unitary to both qubits. The fidelities and Bhattacharyya Coefficients between stages **I** and **II**, and stages **I** and **III** as a function of the rotation angle are shown in Fig. 4.5 for rotation axes, $\hat{x}$, $\hat{y}$, $\hat{z}$, and $\hat{m}$. Panels a)–d) show the fidelity, and panels e)–h) show the Bhattacharyya Coefficient (BC). The open circles show the theoretical expectation for various unitaries. For the fidelity comparison the theoretical model applies perfect unitaries to the imperfect measured state. For the BC comparison the theoretical model applies perfect unitaries to the reconstructed state from stage **I**. We observe very good agreement between the measured and predicted results.

The Bhattacharyya Coefficients from our measured data are shown in Fig. 4.4e)–h). We normalize the measured counts from stages **I** and **III** to give us probability distributions $p_{\text{expt}}^{\mathbf{I}}$ and $p_{\text{expt}}^{\mathbf{III}}$. The coloured data points in Figs. 4.4e)–h) show the BC between these distributions, $BC(p_{\text{expt}}^{\mathbf{I}}, p_{\text{expt}}^{\mathbf{III}})$. The open circles are a theoretical expectation of the BC given the tomographic measurements from stage **I**; for these theoretical values we used state tomography, and thus assumed quantum mechanics, to obtain the expected distribution $p_{\text{th}}^{\mathbf{III}}$ and calculate the expected BC, $BC(p_{\text{expt}}^{\mathbf{I}}, p_{\text{th}}^{\mathbf{III}})$.

Using an analogous procedure to that employed with the fidelity, we estimate the uncertainty in the BC by comparing subsequent measured distributions in stage **I** throughout the experiment, i.e., $BC(p_{\text{expt}}^{\mathbf{I},i}, p_{\text{expt}}^{\mathbf{I},i+1})$. A representative error bar calculated from the data for a set of unitaries around the same axis are shown in Fig. 4.4e)–h). The standard deviation in this quantity over all the data is 0.00005. As before we characterize the difference between the measured and expected BCs as the standard deviation of the quantity $BC(p_{\text{expt}}^{\mathbf{I}}, p_{\text{expt}}^{\mathbf{III}}) - BC(p_{\text{expt}}^{\mathbf{I}}, p_{\text{th}}^{\mathbf{III}})$ which is 0.00009 over all experiments. As before, this value is comparable to the error due to source fluctuations. Data showing the BC between stage **I** and **II** are shown in the appendix along with analogous theoretical comparison. A summary of the BC analysis results are in Table 4.2. The average measured BC is 0.99963 ± 0.00005 $((99.963 \pm 0.005)\%$ of the ideal) across all tested unitaries.
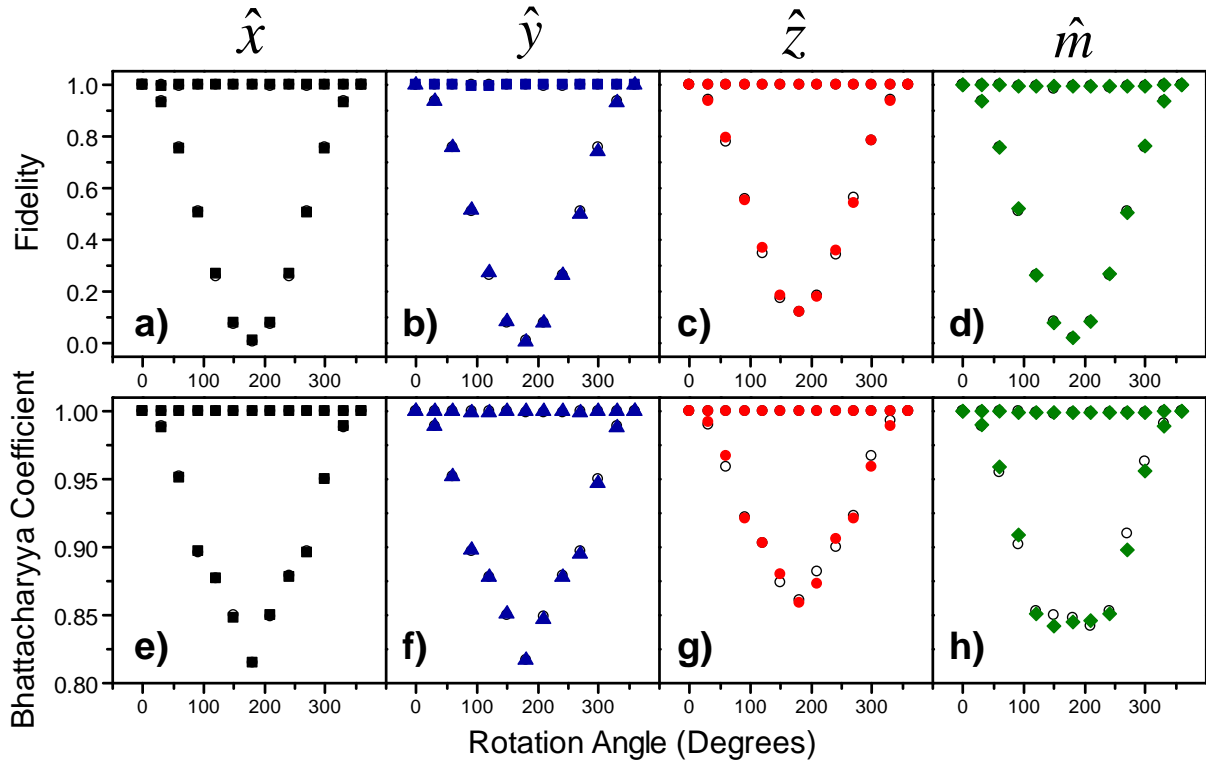
Figure 4.5: Summary of of the experimentally measured fidelity and the Bhattacharyya Coefficient for a wide range of unitaries. Panels a)–d) show the fidelity analysis results for unitary rotations about $\hat{x}$, $\hat{y}$, $\hat{z}$, and $\hat{m}$ axes as functions of rotation angle. The coloured data points are the comparison between stage **I** and stage **III**, and stage **I** and stage **II**. The open circles show the theoretical comparison which takes the state from stage **I** and applies theoretical unitaries. Panels e)–h) show the Bhattacharyya results comparing stage **I** and stage **III**, and stage **I** and stage **II**, in the coloured data points for each of the four axis, with the open circles being the theoretical comparison.

4.5 Conclusion

We have experimentally tested the property of envariance on an entangled two-qubit quantum state. Over a wide range of unitary transformations, we experimentally showed envariance at $(99.66 \pm 0.04)\%$ when measured using the fidelity and $(99.963 \pm 0.005)\%$ using the Bhattacharyya Coefficient. Deviations from perfect envariance are in good agreement with theory and can be explained by our initial state fidelity and fluctuations in the properties of our state. Our results serve as a benchmark for the property of envariance, as improving the envariance of the state significantly would require substantive improvements in source fidelity and stability. It would be interesting to extend tests of envariance to higher dimensional quantum states and specifically to more complex environments.

Chapter 5

Conclusion

We successfully tested two fundamental properties of quantum mechanics, experimentally verifying their characteristics to a high precision and in close agreement with theoretical predictions. This was made possible through improvements to state preparation, including a new alignment method for the Sagnac source and careful optimization of laser and measurement parameters as outlined in chapter two.

In chapter three, we experimentally tested the three families of Bell inequalities recently derived by Wolfe and Yelin [12], following closely to their theoretical predictions. We used the Sagnac source as the quantum platform, and mapped out the largest area of violation of the LHVM to date. This result serves as a benchmark for this area of violation and for general testing of these new inequalities. A next step may be to experiment with other parameterizations of the generalized Bell inequality that were not included in the three families presented by Wolf and Yelin [12].

In chapter four we demonstrated with high precision the property of envariance as described by Zurek in Ref. [15]. The results for this test of envariance are the highest precision to date and therefore serve as a benchmark for this property, which is related to a proof of Born's rule [15]. A next step for this experiment would be a four-qubit experiment that demonstrates a property of envariance used in the proof of Born's rule

called "fine-graining" [1]. It involves the envariance of a two-qubit entangled state under swap in the case of unequal coefficients. Because of the unequal coefficients in the state, in order to test it experimentally it must be rewritten as a three-qutrit, or for experimental convenience, a four-qubit state with equal coefficients. This four qubit state could be tested experimentally under a swap operation. This would effectively test the property of "fine-graining" used in Zurek's proof.

APPENDICES

Appendix A

Replacement Techniques for an Entangled Photon Sagnac Source

A.1 Replacing Elements

In this section tips and procedures for replacing key elements of the Sagnac source without having to perform a complete realignment are included. This is particularly relevant for replacing elements that are damaged or knocked out of place. For some elements this is quite trivial, but for other elements it can be quite challenging.

A.1.1 Replacing the Lens

The ease of replacing the lens greatly depends on whether the thickness of the lens is changing. Before removing anything, place irises in the line of the beam, one directly after the lens and one much further down the beam line. If the replacement lens has the same focal length as the original, then place it in the same spot; align it so it is back-reflected and the beam goes through the exact centre. Some fine tuning on the translation along the beam will be required to find the optimum focus for the light. If the lens is a significantly different thickness, then the beam will be displaced by a different amount than it was

originally, and the rest of the setup after the lens will be misaligned. Depending on the severity of the displacement difference, it may be fastest to realign the entire setup after the lens as outlined in Ref. [34]. To determine this, check to see if there are still coincidence counts coming through. If so, small alignment adjustments may be enough. In this case, adjust the dichroic mirror (if required) such that the beam goes through the centre, then use the hiking boot method to realign the triangle. If there are few to no coincidences, then perform a complete realignment.

A.1.2   Replacing the Dichroic Mirror

Similarly to the lens, changing a dichroic is only a major problem if the displacement of the beam changes. If the new dichroic has caused a different beam shift from the last one, then follow a similar procedure as with the lens. To achieve the proper angle for the dichroic, make use of the grid on the optical table. Otherwise use a rotating mount; back-reflect the dichroic then turn it 45° on a rotation stage.

A.1.3   Replacing the Last HWP

Since the second HWP is after the beam splitter on the optical path, replacing it is relatively simple. Put the new wave plate in roughly the same place as the old one. Ensure the beam goes through the centre of the wave plate and that it is back-reflected. Zero the wave plate to the polarizing beam splitter as discussed in the trouble-shooting section in chapter two.

A.1.4   Replacing the Crystal

The process of replacing a crystal is simplified if it does not involve changing the oven. In this case put the crystal in the oven as close to where the other crystal was and check the back reflection. It will probably need some adjustment, but it should be very close. The oven will also probably need to be translated to maximize coincidences, ensuring that it is equidistant between the two paths. There should be enough coupling to accomplish this

easily, then a fine tuning alignment is typically required for the best results.

If the oven has to be replaced, try to mark out where it was as clearly as possible. Place the new oven there in such a way so that the new crystal is as close as possible to where the old crystal was, i.e., the beam is going straight through the length of the crystal when being pumped from either direction (back-reflect in both directions). Once the crystal is correctly placed, follow the instructions above for alignment. Note: if the triangle mirrors have been altered from alignment, they must be fixed FIRST before replacing the crystal. See Ref. [34] for aligning the mirrors. The section for replacing the mirrors included in this appendix requires the crystal be already correctly in place and back-reflected.

A.1.5 Replacing the Triangle Mirrors

If only one mirror needs replacing, this makes the process easier, and if the mounts for the mirrors are not moved from the original location this also becomes easier. Starting with the best case scenario:

- Only one mirror is being replaced and the mount doesn't need to be moved:
  In this case, assuming the other mirror is aligned properly, remove the mirror that needs to be replaced and put the new mirror in. Making sure the pump is only traveling such that it hits the replaced mirror first, tilt the mirror until the crystal is back-reflected. If this is not possible, it means the mount for the replaced mirror has been disturbed. If back-reflection is possible, the paths should be overlapping, and walking the mirrors as described in the alignment methods should be sufficient.

- Only one mirror is being replaced and the mount must be moved or has been disturbed:
  Level the mirror being replaced (i.e., put an iris in aligned to the incoming beam, place the mirror as far from the iris as possible, and tilt until the beam is reflected perfectly back through the iris). Now place the mirror (don't tilt) such that the crystal is back-reflected (pump in one direction, hitting the replaced mirror first). Now walk the mirrors according to the alignment methods.

- Both mirrors need to be replaced, but the mounts don't need to be moved:
  Place the new mirrors in, trying not to disturb the mounts. Tilt the mirrors one at a time (pumping in different polarizations for each), to back-reflect the crystal. If you are successful, proceed to walk the mirrors according to the alignment method. If not, the mounts have been disturbed.

- Both mirrors need to be replaced and both mounts need to be moved (or have been disturbed):
  Level one mirror and place so as to back-reflect the crystal (again pumping with the appropriate polarization). Do the same for the other mirror, then walk the mirrors as described by the alignment methods.

A.1.6   Replacing the Polarizing Beam Splitter

This is the most difficult element to replace, and this is due to the number of degrees of freedom that have to be accounted for to achieve alignment. This procedure is easiest if the triangle mirrors haven't been touched. Assuming the mirrors haven't been touched, start with placement: place so that the incoming beam is approximately in the centre of the PBS and the reflected port goes through the centre of the HWP in the triangle. Check to make sure that the reflected beam going into the coupler goes through the centre of the filter. Now back-reflect along the line of the incoming beam. The last degree of back-reflection is in the direction of the reflected beam going into the triangle. Use the back-reflection of the crystal to align this direction. If the mirrors have been moved then placing becomes a little trickier as the only reference is the incoming beam and the HWP in the triangle, but it is still possible. For back-reflecting the last degree of freedom use the HWP in the triangle's back-reflection. This is all much easier with reference irises placed along all the different PBS ports to help with placement.

References

[1] M. Born, Z. Phys. **38**, 803 (1926).

[2] R. Jozsa, J. Mod. Opt. **41**, 2315 (1994).

[3] A. Bhattacharyya , Bulletin of the Calcutta Mathematical Society **35**, 99 (1943).

[4] B. E. Kane, Nature **393**, 133 (1998)

[5] J. Majer J. M. Chow, J. M. Gambetta, Jens Koch, B. R. Johnson, J. A. Schreier, L. Frunzio, D. I. Schuster, A. A. Houck1, A. Wallraff, A. Blais, M. H. Devoret, S. M. Girvin and R. J. Schoelkop, Nature **449**, 443 (2007)

[6] E. Knill, R. Laflamme and G. J. Milburn, Nature **409**, 46 (2001).

[7] J. L. O'Brien, Science **318**, 1567 (2007)

[8] M. A. Nielsen and I. L. Chuang, *Quantum Computation and Quantum Information* (Cambridge University Press, 2010).

[9] H. Poincaré, Theorie mathematique de la lumiere, vol. 2, (G. Carre, Paris), (1892) Chap. 12.

[10] The tangle is the square of the concurrence. V. Coffman, J. Kundu, and W.K. Wootters, Phys. Rev. A **61**, 052306 (2000).

[11] J. F. Clauser, M. A. Horne, A. Shimony, and R. A. Holt, Phys. Rev. Lett. **23**, 880 (1969).

[12] E. Wolfe and S. F. Yelin, Phys. Rev. A **86**, 012123 (2012).

[13] A. Cabello, Phys. Rev. A **72**, 012113 (2005).

[14] W. H. Zurek, Phys. Rev. Lett. **90**, 120404 (2003).

[15] W. H. Zurek, Phys. Rev. A **71**, 052105 (2005).

[16] M. Ježek, J. Fiurášek, and Z. Hradil, Phys. Rev. A **68**, 012305 (2003).

[17] G. C. Stokes, Trans. Cambr. Phil. Soc. 9, 399 (1852).

[18] C. Kurtsiefer, T. Pfau and J. Mlynek, Nature **386**, 150 (1997).

[19] L. G. Lutterbach and L. Davidovich, Phys. Rev. Lett. **78**, 2547 (1997).

[20] C. T. Bodendorf, G. Antesberger, M. S. Kim, and H. Walther, Phys. Rev. A **57**, 1371 (1998).

[21] D. F. V. James, P. G. Kwiat, W. J. Munro and A. G. White, Phys. Rev. A. **64**, 052312 (2001)

[22] P. G. Kwiat, K. Mattle, H. Weinfurter, A. Zeilinger, A. V. Sergienko and Y. Shih, Phys. Rev. Lett. **75**, 4337 (1995).

[23] P. G. Kwiat, E. Waks, A. G. White, I. Appelbaum and P. H. Eberhard, Phys. Rev. A **60** 773(R) (1999).

[24] C. K. Hong and L. Mandel, Phys. Rev. A **31**, 2409 (1985).

[25] Z. Y. Ou, L. J. Wang and L. Mandel, Phys. Rev. A **40**, 1428 (1989).

[26] J. A. Armstrong, N. Bloemgergen, J. Ducuing and P. S. Pershan, Phys. Rev. **127** 1918 (1962).

[27] D. S. Hum and M. M. Fejer, Comptes Rendus Physique **8**, 180 (2007).

[28] N. K. Langford, *Encoding, manipulating and measuring quantum information in optics*, Ph.D. thesis, University of Queensland (2007).

[29] Bao-Sen Shi and A. Tomita, Phys. Rev. A, **69**, 013803 (2004)

[30] T. Kim, M. Fiorentino, and F. N. C. Wong, Phys. Rev. A, **73**, 012316 (2006).

[31] F. N. C. Wong, J. H. Shapiro, and T. Kim, Laser Physics, **16**, 1517 (2006).

[32] A. Fedrizzi, T. Herbst, A. Poppe, T. Jennewein and A. Zeilinger, Opt. Express, **15**, 15377 (2007).

[33] A. Predojević, S. Grabher, and G. Weihs, Opt. Express, **20**, 25022 (2012).

[34] D. R. Hamel, *Realization of novel entangled photon sources using periodically poled materials*, Masters thesis, University of Waterloo (2010).

[35] A. Cabello, Phys. Rev. A **72**, 050101(R) (2005)

[36] J. S. Bell, Physics **1**, 195 (1964).

[37] A. J. Leggett, Found. Phys. **33**, 1469 (2003).

[38] G. Svetlichny, Phys. Rev. D **35**, 3066 (1987).

[39] P. Hyllus, O. Gühne, D. Bruß, and M. Lewenstein, Phys. Rev. A **72**, 012321 (2005).

[40] A. K. Ekert, Phys. Rev. Lett. **67**, 661 (1991).

[41] A. Acín et al., Phys. Rev. Lett. **98**, 230501 (2007).

[42] G. Brassard, Found. Phys. **33**, 1593 (2003).

[43] S. Pironio et al., Nature **464**, 1021 (2010).

[44] R. Prevedel, Y. Lu, W. Matthews, R. Kaltenbaek, and K. J. Resch, Phys. Rev. Lett. **106**, 110505 (2011).

[45] S. J. Freedman and J. F. Clauser, Phys. Rev. Lett. **28**, 938 (1972).

[46] A. Aspect, J. Dalibard, and G. Roger, Phys. Rev. Lett. **49**, 1804 (1982).

[47] Z. Y. Ou and L. Mandel, Phys. Rev. Lett. **61**, 50 (1988).

[48] Y. H. Shih and C. O. Alley, Phys. Rev. Lett. **61**, 2921 (1988).

[49] G. Weihs, T. Jennewein, C. Simon, H. Weinfurter, and A. Zeilinger, Phys. Rev. Lett. **81**, 5039 (1998).

[50] M. A. Rowe, D. Kielpinski, V. Meyer, C. A. Sackett, W. M. Itano, C. Monroe, and D. J. Wineland, Nature **409**, 791 (2001).

[51] S. Gröblacher, T. Paterek, R. Kaltenbaek, C. Brukner, M. Żukowski, M. Aspelmeyer, and A. Zeilinger, Nature **446**, 871 (2007).

[52] M. Ansmann, H. Wang, R. C. Bialczak, M. Hofheinz, E. Lucero, M. Neeley, A. D. O'Connell, D. Sank, M. Weides, J. Wenner, A. N. Cleland, and J. M. Martinis, Nature **461**, 504 (2009).

[53] J. M. Chow, L. DiCarlo, J. M. Gambetta, A. Nunnenkamp, L. S. Bishop, L. Frunzio, M. H. Devoret, S. M. Girvin, and R. J. Schoelkopf, Phys. Rev. A **81**, 062325 (2010).

[54] D.M. Greenberger, M.A. Horne, and A. Zeilinger, in *Bells Theorem, Quantum Theory and Conceptions of the Universe*, edited by M. Kafatos (Kluwer Academic Publishers, Dordrecht 1989) p73.

[55] N. D. Mermin, Phys. Rev. Lett. **65**, 1838 (1990).

[56] M. Ardehali, Phys. Rev. A **46**, 5375 (1992).

[57] D. N. Klyshko, Phys. Lett. A **172**, 399 (1993).

[58] D. Bouwmeester, J.-W. Pan, M. Daniell, H. Weinfurter, and A. Zeilinger, Phys. Rev. Lett. **82**, 1345 (1999).

[59] J.-W. Pan, D. Bouwmeester, M. Daniell, H. Weinfurter, and A. Zeilinger, Nature **403**, 515 (2000).

[60] P. Walther, M. Aspelmeyer, K. J. Resch, and A. Zeilinger, Phys. Rev. Lett. **95**, 020403 (2005).

[61] J. Lavoie, R. Kaltenbaek, and K. J. Resch, New J. Phys. **11**, 073051 (2009).

[62] N. Gisin, Phys. Lett. A **201**, 151 (1996).

[63] A. C. Dada, J. Leach, G. S. Buller, M. J. Padgett, and E. Andersson, Nature Phys. **7**, 677 (2011).

[64] T. Kim, M. Fiorentino, and F. N. C. Wong, Phys. Rev. A **73**, 012316 (2006).

[65] A. Fedrizzi, T. Herbst, A. Poppe, T. Jennewein, and A. Zeilinger, Optics Express **15**, 15377 (2007).

[66] D. N. Biggerstaff, et al., Phys. Rev. Lett. **103**, 240504 (2009).

[67] R. Jozsa, J. Mod. Opt. **41**, 2315 (1994).

[68] D.F.V. James, P.G. Kwiat, W.J. Munro, and A.G. White, Phys. Rev. A **64**, 052312 (2001).

[69] W. H. Zurek, Rev. Mod. Phys. **75**, 715 (2003)
Calcutta Mathematical Society **35**, 99 (1943).

[70] W.H. Zurek, Physics Today **44**(10), 36 (1991).

[71] M. Schlosshauer, Rev. Mod. Phys. **76**, 1267-1305 (2004)

[72] L. Landau, Z. Phys. **45**, 430 (1927).

[73] M. Schlosshauer and A. Fine, Found. Phys. **35**, 197 (2005).

[74] U. Mohrhoff, Int. J. Quantum Inf. **2**, 221 (2004)

[75] H. Barnum, No-signalling-based version of Zurek's derivation of quantum probabilities: A note on ""Environment-assisted invariance, entanglement, and probabilities in quantum physics", eprint quant-ph/0312150 (2008)